

PAPER

Investigation of the density shoulder formation by using self-consistent simulations of plasma turbulence and neutral kinetic dynamics

To cite this article: D. Mancini *et al* 2021 *Nucl. Fusion* **61** 126029

View the [article online](#) for updates and enhancements.

You may also like

- [Scrape-off layer transport and filament characteristics in high-density tokamak regimes](#)
N. Vianello, D. Carralero, C.K. Tsui et al.
- [Dependence of upstream SOL density shoulder on divertor neutral pressure observed in L-mode and H-mode plasmas in the EAST superconducting tokamak](#)
N. Yan, L. Chen, G.S. Xu et al.
- [Investigation into the formation of the scrape-off layer density shoulder in JET ITER-like wall L-mode and H-mode plasmas](#)
A. Wynn, B. Lipschultz, I. Cziegler et al.

Investigation of the density shoulder formation by using self-consistent simulations of plasma turbulence and neutral kinetic dynamics

D. Mancini^{1,2,*}, P. Ricci², N. Vianello³ , M. Giacomin²  and A. Corrado² 

¹ Università degli studi della Tuscia, Largo dell'Università s.n.c., 01100 Viterbo, Italy

² Ecole Polytechnique Fédérale de Lausanne (EPFL), Swiss Plasma Center (SPC), CH-1015 Lausanne, Switzerland

³ Consorzio RFX, CNR, ENEA, INFN, Università di Padova, Acciaierie Venete SpA, Corso Stati Uniti 4, 35127, Padova, Italy

E-mail: davide.mancini@studenti.unitus.it

Received 24 July 2021, revised 4 October 2021

Accepted for publication 18 October 2021

Published 3 November 2021



CrossMark

Abstract

Simulations of plasma turbulence in a lower single-null magnetic configurations are presented. The plasma dynamics is modelled by the drift-reduced two-fluid Braginskii equations that are coupled with a kinetic model for a single neutral species that considers ionization, charge-exchange, recombination and elastic collisions. The effect of increased core fuelling on the plasma scrape-off layer (SOL) density and temperature profile is investigated. The increase in core fuelling leads to an increase of the e-folding length in the near SOL and, in the far SOL, to an increase of the plasma density. These results are in agreement with experimental measurements, and in particular with the observations of the formation of a density shoulder in high-fuelling scenarios. The physical mechanisms underlying the increase of the far SOL density are analysed comparing parallel and perpendicular fluxes in the SOL and considering also simulations with similar parameters but without neutrals. Despite the increase of the blob size, the increase of the far SOL density observed at high-fuelling rates is found to be mainly caused by the strong decrease of parallel transport, due to the cooling of electrons resulting from ionization events.

Keywords: plasma turbulence, neutral interactions, GBS, shoulder formation

(Some figures may appear in colour only in the online journal)

1. Introduction

The boundary of fusion plasma devices is characterized by a significant presence of neutral particles, resulting either from local gas injection or from plasma recycling at the vessel walls. The neutrals interact with plasma through different reactions like ionization, charge-exchange, recombination and elastic collisions, playing a crucial role in providing the power

and momentum loss mechanisms needed to reach plasma detachment [1–3], in the L–H mode transition and in the enhancement of edge plasma turbulence [4], possibly through a reduction of the amplitude of zonal flows [5] or by sustaining filamentary transport thanks to local ionization [6]. The latter two mechanisms have been proposed also as possible candidates for the formation of the *density shoulder*, i.e. the flattening of the scrape-off layer (SOL) density profile at the tokamak outer mid-plane (OMP) observed when core density is increased by increase in fuelling [7].

* Author to whom any correspondence should be addressed.

Even if the formation of the density shoulder is the subject of a number of experimental investigations carried out in several devices [7–10], there is still debate about the physical mechanisms behind it [9, 11, 12]. As a matter of fact, a proper modelling of plasma–neutrals interactions in a full tokamak turbulent simulation is generally thought necessary to gain the fundamental insights on this phenomenon. Since flatter density profiles are often observed to affect the transport in the SOL and the fluxes to the vessel wall [11, 13], the understanding of the density shoulder formation is of crucial importance for the design of plasma facing components in high-density devices.

While the study of the interaction of plasma and neutrals is most often approached by using fluid models for the plasma, where perpendicular transport is modelled as a diffusive process, and kinetic Monte-Carlo models for the neutral dynamics (see, e.g. the SOLPS-ITER [14] and SOLEDGE2D [15] codes), different approaches have been recently suggested in order to incorporate neutral dynamics into turbulence boundary codes that are, most often, based on the drift-reduced Braginskii equations for the plasma [16, 17]. The plasma turbulence code TOKAM3X [18, 19] has been coupled with SOLEDGE2D [15]. The resulting code, SOLEDGE3X [20], can address the plasma turbulent dynamics and the neutral physics using a Monte Carlo approach to the neutral kinetic equation, based on the EIRENE code [21], giving insight on turbulent impurity transport [22]. A fluid-diffusive model for the neutrals is implemented in nHESEL and two-dimensional simulations accounting for both atomic and molecular hydrogen have been performed [6, 23]. In BOUT++ a single component fluid model for the neutrals is coupled to a three-dimensional plasma turbulent model [24, 25]. The neutral dynamics [26] is also implemented in the GBS code [27, 28] by numerically discretizing the kinetic equation for the neutral species integrated along the neutral characteristics. By focussing on limited configurations, GBS simulations have allowed insights on the drop of the electron temperature in the proximity of the limiter plates [29] and on the impact of neutral fluctuations on gas-puff imaging [30].

In this paper, we present and discuss the results of the first simulations of GBS in a lower single-null configuration, with the neutral dynamics included. These simulations leverage recent effort to extend the capabilities of GBS to simulate plasma turbulence in arbitrary magnetic configurations in a full torus, thus retaining the SOL–edge–core interplay [31, 32]. Following [26], neutral dynamics is simulated by considering a single mono-atomic neutral species that interacts with the plasma through ionization, charge–exchange, recombination and elastic electron–neutral collisions. The solution of a kinetic equation for the neutrals allows us to self-consistently simulate the neutral dynamics, without making assumptions on neutrals transport coefficients as typically required by the fluid approaches [6]. Plasma profiles are evolved without separation between equilibrium and fluctuating quantities, as they result from the self-consistent interplay of the sources of plasma density and heat, perpendicular turbulent transport, parallel flow and losses at the vessels walls.

A scan of simulations is described, with increasing core fuelling. We show that neutrals affect both the plasma profiles and turbulence properties. In particular, associated with an increase of fuelling, an increase of the plasma resistivity is observed. This leads to an increase of the e-folding length in the near SOL. In the far SOL, an increase of the fuelling rate leads to an increase in plasma density. This result is in agreement with experimental evidences when the density shoulder forms in high-fuelling scenarios. Associated with the increased density an increase of the blob size and a decrease in blob radial velocity are observed. On the other hand, by comparing parallel and perpendicular fluxes in the SOL, the increase in far SOL density observed at high fuelling is shown to be mainly due to the strong decrease of parallel transport. This is caused by the electron cooling, resulting from ionization reactions in the core and in the SOL region, that reduce the plasma outflow speed to the wall.

The article is structured as follows. In section 2 we introduce the model we use to self-consistent simulate plasma turbulence and neutral dynamics as well as its implementation in GBS. Section 3 provides an overview of the results obtained from a scan of simulations where we vary the core fuelling. The physical mechanisms behind the formation of the density shoulder are analysed in section 4. The conclusions follow.

2. Simulations model

Our study is based on simulations carried out with the GBS code [27, 28, 33], a three-dimensional, flux-driven, two-fluid code used to study plasma turbulence in the tokamak boundary. Initially developed to simulate basic plasma physics experiments [17, 34], GBS was then ported to the limited configuration of tokamaks [35] where the plasma model was coupled to a self-consistent kinetic neutral model [26]. Thanks to the improvement of the numerical scheme [33], GBS was enabled to carry out simulations in diverted configurations, encompassing the full plasma volume in order to avoid an artificial boundary with the tokamak core [31]. The results we discuss in the present paper are based on the first simulations in a diverted configuration where the plasma fluid model is coupled with a kinetic model for neutrals. We first describe the plasma and then the neutral model.

2.1. The plasma model

The plasma is modelled by using the Braginskii equations [36], assuming that the electron mean free path is shorter than the typical length scales of turbulence in the parallel direction, $\lambda_e \ll L_{\parallel} \sim 2\pi qR$. In addition, we make use of the drift approximation [37] for the particle velocity, which is valid if turbulent scale lengths in the perpendicular direction are larger than the ion Larmor radius, $k_{\perp}\rho_i \ll 1$, and typical turbulent time scales are slower than the ion cyclotron time scale, Ω_{ci} . These conditions are typically satisfied in the SOL of L-mode discharges. Since we focus our attention on the plasma interaction with the neutral particles, for simplicity we neglect electromagnetic effects and we use the Boussinesq approximation.

This leads to the following set of equations

$$\nabla_{\perp}^2 \phi = \omega - \frac{\nabla_{\perp}^2 T_i}{e}. \quad (7)$$

$$\begin{aligned} \frac{\partial n}{\partial t} = & -\frac{1}{B}[\phi, n] + \frac{2}{eB} [C(p_e) - enC(\phi)] - \nabla_{\parallel}(nv_{\parallel e}) \\ & + D_n \nabla_{\perp}^2 n + \nu_{iz} n_n - \nu_{rec} n, \end{aligned} \quad (1)$$

$$\begin{aligned} \frac{\partial \omega}{\partial t} = & -\frac{1}{B}[\phi, \omega] - v_{\parallel i} \nabla_{\parallel} \omega + \frac{eB^2}{m_i n} \nabla_{\parallel} j_{\parallel} \\ & + \frac{2B}{m_i n} C(p_e + p_i) + D_{\omega} \nabla_{\perp}^2 \omega - \frac{n_n}{n} \nu_{cx} \omega, \end{aligned} \quad (2)$$

$$\begin{aligned} \frac{\partial v_{\parallel e}}{\partial t} = & -\frac{1}{B}[\phi, v_{\parallel e}] - v_{\parallel e} \nabla_{\parallel} v_{\parallel e} \\ & + \frac{e}{m_e} \left(\frac{j_{\parallel}}{\sigma_{\parallel}} + \nabla_{\parallel} \phi - \frac{1}{en} \nabla_{\parallel} p_e - \frac{0.71}{e} \nabla_{\parallel} T_e \right) \\ & + \frac{4}{3m_e n} \eta_{0,e} \nabla_{\parallel}^2 v_{\parallel e} + D_{v_{\parallel e}} \nabla_{\perp}^2 v_{\parallel e} \\ & + \frac{n_n}{n} (\nu_{en} + 2\nu_{iz}) (v_{\parallel n} - v_{\parallel e}), \end{aligned} \quad (3)$$

$$\begin{aligned} \frac{\partial v_{\parallel i}}{\partial t} = & -\frac{1}{B}[\phi, v_{\parallel i}] - v_{\parallel i} \nabla_{\parallel} v_{\parallel i} - \frac{1}{m_i n} \nabla_{\parallel} (p_e + p_i) \\ & + \frac{4}{3m_i n} \eta_{0i} \nabla_{\parallel}^2 v_{\parallel i} \\ & + D_{v_{\parallel i}} \nabla_{\perp}^2 v_{\parallel i} + \frac{n_n}{n} (\nu_{iz} + \nu_{cx}) (v_{\parallel n} - v_{\parallel i}), \end{aligned} \quad (4)$$

$$\begin{aligned} \frac{\partial T_e}{\partial t} = & -\frac{1}{B}[\phi, T_e] - v_{\parallel e} \nabla_{\parallel} T_e + \frac{2}{3} T_e \left[0.71 \frac{\nabla_{\parallel} j_{\parallel}}{en} - \nabla_{\parallel} v_{\parallel e} \right] \\ & + \frac{4}{3} \frac{T_e}{eB} \left[\frac{7}{2} C(T_e) + \frac{T_e}{n} C(n) - eC(\phi) \right] \\ & + \chi_{\parallel e} \nabla_{\parallel}^2 T_e + D_{T_e} \nabla_{\perp}^2 T_e + s_{T_e} \\ & - \frac{n_n}{n} \nu_{en} m_e \frac{2}{3} v_{\parallel e} (v_{\parallel n} - v_{\parallel e}) \\ & + \frac{n_n}{n} \nu_{iz} \left[-\frac{2}{3} E_{iz} - T_e + m_e v_{\parallel e} \left(v_{\parallel e} - \frac{4}{3} v_{\parallel n} \right) \right], \end{aligned} \quad (5)$$

$$\begin{aligned} \frac{\partial T_i}{\partial t} = & -\frac{1}{B}[\phi, T_i] - v_{\parallel i} \nabla_{\parallel} T_i \\ & + \frac{4}{3} \frac{T_i}{eB} \left[C(T_e) + \frac{T_e}{n} C(n) - eC(\phi) \right] - \frac{10}{3} \frac{T_i}{eB} C(T_i) \\ & + \frac{2}{3} T_i \left[(v_{\parallel i} - v_{\parallel e}) \frac{\nabla_{\parallel} n}{n} - \nabla_{\parallel} v_{\parallel e} \right] \\ & + \chi_{\parallel i} \nabla_{\parallel}^2 T_i + D_{T_i} \nabla_{\perp}^2 T_i + s_{T_i} \\ & + \frac{n_n}{n} (\nu_{iz} + \nu_{cx}) \left[T_n - T_i + \frac{1}{3} (v_{\parallel n} - v_{\parallel i})^2 \right], \end{aligned} \quad (6)$$

In (1)–(7), $[\phi, f] = \mathbf{b} \cdot (\nabla \phi \times \nabla f)$ is the $\mathbf{E} \times \mathbf{B}$ convective operator, $C(f) = B/2[\nabla \times (\mathbf{b}/B)] \cdot \nabla f$ is the curvature operator, $\nabla_{\parallel} f = \mathbf{b} \cdot \nabla f$ is the parallel gradient, and $\nabla_{\perp}^2 f = \nabla \cdot [(\mathbf{b} \times \nabla f) \times \mathbf{b}]$ is the perpendicular Laplacian, with $\mathbf{b} = \mathbf{B}/B$ the unit vector in the direction of the magnetic field. The toroidally symmetric magnetic field is written in terms of the flux function ψ ,

$$\mathbf{B} = RB_{\varphi} \nabla \varphi + \nabla \psi \times \nabla \varphi, \quad (8)$$

with $\nabla \varphi$ the toroidal direction, B_{φ} the toroidal magnetic field and $\nabla \psi$ is the direction orthogonal to the flux surfaces. In this work, the simulation domain encompasses the whole tokamak plasma volume, with a rectangular poloidal cross section of vertical and radial extension L_Z and L_R , as done for the first time in [32] and with close similarity to the TCV tokamak [38]. It is therefore convenient to express all the spatial operators in (1)–(7) and evolve the plasma and neutral model in the cylindrical coordinate system (R, φ, Z) , being R the radial distance from the tokamak axis of symmetry and Z the vertical coordinate [31]. For the analysis we also use a flux aligned coordinate system $(\nabla \psi, \nabla \chi, \nabla \varphi)$, where $\nabla \chi = \nabla \varphi \times \nabla \psi$.

While (1)–(7) are presented in physical units, they are implemented in GBS in dimensionless form. Plasma and neutral densities are normalized to the reference density n_0 , electron and ion temperatures to the reference temperature T_{e0} and T_{i0} and velocities to the sound speed $c_{s0} = \sqrt{T_{e0}/m_i}$. The norm of the magnetic field B is normalized to the field value on the magnetic axis B_0 , perpendicular lengths to the ion sound Larmor radius $\rho_{s0} = c_{s0}/\Omega_{ci}$, where $\Omega_{ci} = eB_0/m_i$, parallel lengths to the tokamak major radius R_0 , and time to $t_0 = R_0/c_{s0}$. By normalizing equations (1)–(7), the following dimensionless parameters that regulate the system dynamics are identified: the normalized ion Larmor radius, $\rho_* = \rho_{s0}/R_0$, the ion to electron temperature ratio, $\tau = T_{i0}/T_{e0}$, and the normalized Spitzer resistivity $\nu = e^2 n_0 R_0 / (m_i c_{s0} \sigma_{\parallel}) = \nu_0 T_e^{-3/2}$, with

$$\begin{aligned} \sigma_{\parallel} = & \left(1.96 \frac{n_0 e^2 \tau_e}{m_e} \right) n = \left(\frac{5.88}{4\sqrt{2\pi}} \frac{(4\pi\epsilon_0)^2}{e^2} \frac{T_{e0}^{3/2}}{\lambda \sqrt{m_e}} \right) (T_e)^{3/2} \\ \nu_0 = & \frac{4\sqrt{2\pi}}{5.88} \frac{e^4}{(4\pi\epsilon_0)^2} \frac{\sqrt{m_e} R_0 n_0 \lambda}{m_i c_{s0} T_{e0}^{3/2}} \end{aligned} \quad (9)$$

The expression of electron and ion viscosities, η_{0e} and η_{0i} in (3) and (4), as well as the electron and ion parallel thermal conductivities, χ_{0e} and χ_{0i} in (5) and (6), can be found in [39]. For this work, the normalized viscosities, $\tilde{\eta}_{0e} = \eta_{0e} m_e / (0.73 n_0 t_0 R_0)$ and $\tilde{\eta}_{0i} = \eta_{0i} m_i / (0.96 n_0 t_0 R_0)$, and the normalized parallel thermal conductivities, $\tilde{\chi}_{\parallel e} = \chi_{\parallel e} / (1.58 n_0 t_0 R_0)$ and $\tilde{\chi}_{\parallel i} = \chi_{\parallel i} / (1.94 n_0 t_0 R_0)$, are all taken as constant. In (1)–(6) the normalized diffusion coefficients $\tilde{D}_f = D_f / (\rho_{s0} c_{s0} \rho_*)$, for the field f , are introduced for numerical stability.

We describe the interaction of the plasma with the neutrals by considering ionization, charge–exchange, elastic collisions

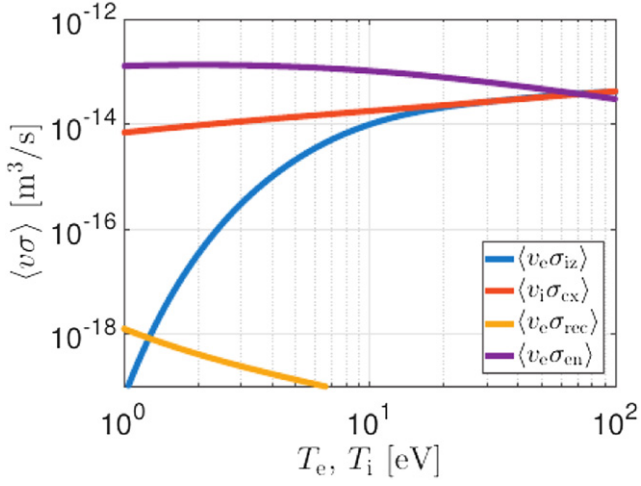


Figure 1. Reaction rates for ionization, charge–exchange, elastic electron–neutral collisions and recombination, for plasma density $n = 5 \times 10^{19} \text{ m}^{-3}$.

and recombination processes that are modelled through Krook operators with collision frequencies:

$$\begin{aligned} \nu_{iz} &= n_e \langle v_e \sigma_{iz}(v_e) \rangle_e \\ \nu_{cx} &= n_i \langle v_i \sigma_{cx}(v_i) \rangle_i \\ \nu_{en} &= n_e \langle v_e \sigma_{en}(v_e) \rangle_e \\ \nu_{rec} &= n_e \langle v_e \sigma_{rec}(v_e) \rangle_e \end{aligned} \quad (10)$$

In (10) ionization, elastic collisions and recombination reaction rates are averaged over the electron distribution function, neglecting the neutral with respect to the electron velocity. The charge–exchange cross section is averaged over the ion distribution function, depending weakly on the relative velocity of ions and neutrals [40]. The reaction rates, taken from the *OpenADAS* database [41] as the solution of a collisional-radiative model, are shown in figure 1. We assume that electrons resulting from ionization processes have a Maxwellian distribution function with average parallel velocity that corresponds to the neutral velocity v_n , because of the electron to neutral mass ratio, and temperature $T_{e,iz} = T_e/2 - E_{iz}/3 + m_e v_e^2/6 - m_e v_n^2/3$, obtained from energy conservation with E_{iz} the average energy loss in an ionization process. Also for the elastic collisions with neutrals, the emission is according to a Maxwellian distribution function, always with average velocity v_n and with temperature $T_{e,en} = T_e + m_e(v_e^2 - v_n^2)/3$, also obtained from energy consideration and taking into account that neutrals are considerably heavier than electrons.

In contrast to previous simulations in diverted configurations [31, 42], herein the fuelling is entirely the result of neutral ionization processes, while s_{T_e} and s_{T_i} are the external temperature source terms in (5) and (6). We define S_n , S_{T_e} and S_{T_i} as the total density, electron temperature and ion temperature sources integrated over the area inside the last closed flux surface (LCFS), i.e.

$$S_n = \int_{A_{LCFS}} s_n^n(R, Z) dR dZ, \quad (11)$$

$$S_{T_e} = S_{T_e}^{\text{cost}} + S_{T_e}^n = \int_{A_{LCFS}} [s_{T_e}(R, Z) + s_{T_e}^n(R, Z)] dR dZ \quad (12)$$

and

$$S_{T_i} = S_{T_i}^{\text{cost}} + S_{T_i}^n = \int_{A_{LCFS}} [s_{T_i}(R, Z) + s_{T_i}^n(R, Z)] dR dZ. \quad (13)$$

The plasma density source resulting from ionization processes is expressed as $s_n^n = n_n \nu_{iz}$ (see (1)), while $s_{T_e}^n = \{n_n \nu_{iz} [-2E_{iz}/3 - T_e + m_e v_{\parallel,e} (v_{\parallel,e} - 4v_{\parallel,n}/3)] - 2n_n \nu_{en} m_e v_{\parallel,e} (v_{\parallel,n} - v_{\parallel,e})/3\}/n$ and $s_{T_i}^n = \{n_n (\nu_{iz} + \nu_{cx}) [T_n - T_i + (v_{\parallel,n} - v_{\parallel,i})^2/3]\}/n$ are the electron and ion contribution to the temperatures evolution due to the interaction with the neutrals (see (5) and (6)). We also define the external electron heat source as $s_{p_e} = n s_{T_e}$ and the electron heat source due to the interaction with neutrals as $s_{p_e}^n = n s_{T_e}^n + T_e s_n^n$. The ion heat sources are defined analogously. The total heat source can therefore be expressed as

$$\begin{aligned} S_P &= \int_{A_{LCFS}} \left[s_{p_e}(R, Z) \right. \\ &\quad \left. + s_{p_e}^n(R, Z) + s_{p_i}(R, Z) + s_{p_i}^n(R, Z) \right] dR dZ. \end{aligned} \quad (14)$$

At the divertor target plates (bottom wall of the domain) we implement the pre-sheath set of magnetic boundary conditions derived in [43] in the cold ion case and generalised by [44] to take into account finite ion temperature:

$$v_{\parallel i} = \pm c_s \sqrt{1 + \frac{T_i}{T_e}} \quad (15)$$

$$v_{\parallel e} = \pm c_s \max \left\{ \exp \left(\Lambda - \frac{e\phi}{T_e} \right), \exp(\Lambda) \right\} \quad (16)$$

$$\partial_Z n = \mp \frac{n}{c_s \sqrt{1 + \frac{T_i}{T_e}}} \partial_Z v_{\parallel i} \quad (17)$$

$$\partial_Z \phi = \mp \frac{m_i c_s}{e \sqrt{1 + \frac{T_i}{T_e}}} \partial_Z v_{\parallel i} \quad (18)$$

$$\partial_Z T_e = \partial_Z T_i = 0 \quad (19)$$

$$\omega = -\frac{m_i}{e} \frac{1}{1 + \frac{T_i}{T_e}} \left[(\partial_Z v_{\parallel i})^2 \pm \frac{c_s}{\sqrt{1 + \frac{T_i}{T_e}}} \partial_{ZZ}^2 v_{\parallel i} \right], \quad (20)$$

where the plus (minus) sign refers to case of the magnetic field pointing towards (away) from the target and $\Lambda = \log \sqrt{m_i/(2\pi m_e)} \simeq 3$ for hydrogen plasma. The same boundary conditions are used also for the top wall, while for the left and right walls we use simplified boundary conditions where the electrostatic potential is set to $e\phi = \Lambda T_e$ and we impose vanishing derivatives in the direction perpendicular to the wall for the other quantities.

The numerical implementation of (1)–(6) is described in [28]. The system of equations is advanced by using a standard fourth-order Runge–Kutta algorithm, while the spatial operators are discretized by a fourth-order centred finite differences scheme, except for the Poisson brackets that are discretized by using the Arakawa scheme [45]. Poisson equation (7) is solved by a direct inversion of the perpendicular Laplacian operator through LU factorisation using the MUMPS library [46].

2.2. The neutral model

Following [26], we base our model on a kinetic description of a mono-atomic neutral species, i.e.

$$\frac{\partial f_n}{\partial t} + \mathbf{v} \cdot \frac{\partial f_n}{\partial \mathbf{x}} = -\nu_{iz} f_n - \nu_{cx} \left(f_n - \frac{n_n}{n_i} f_i \right) + \nu_{rec} f_i, \quad (21)$$

where f_n and f_i are the neutral and ion distribution functions. Previous studies based on GBS simulations that include the neutral dynamics have been carried out in limited configurations, shedding light on the effect of neutrals on the temperature drop along the magnetic field line [29], as well as on the effect of neutral fluctuations on gas puff imaging [30]. Also in limited configuration, the mass conservation properties of the model have been recently studied [47]. Here, we extend the work in [26] by allowing the self-consistent GBS simulation of neutrals and plasma in diverted configurations for the first time.

As boundary conditions for (21), we consider the following distribution function for the neutrals flowing from the wall towards the plasma

$$\begin{aligned} f_n(\mathbf{x}_b, \mathbf{v}, t) = & [1 - \alpha_{\text{refl}}(\mathbf{x}_b)] \Gamma_{\text{out}}(\mathbf{x}_b, \mathbf{v}, t) \chi_{\text{in}}(\mathbf{x}_b, \mathbf{v}, t) \\ & + \alpha_{\text{refl}}(\mathbf{x}_b) [f_n(\mathbf{x}_b, \mathbf{v} - 2\mathbf{v}_p, t) \\ & + f_i(\mathbf{x}_b, \mathbf{v} - 2\mathbf{v}_p, t)], \end{aligned} \quad (22)$$

where $\mathbf{v}_p = v_p \hat{\mathbf{n}}$ is the velocity perpendicular to the boundary, $\hat{\mathbf{n}}$ is the unit vector normal to the wall and pointing towards the plasma volume and \mathbf{x}_b a point on the wall boundary. The distribution function in (22) takes into account that a fraction of the ions, $\alpha_{\text{refl}}(\mathbf{x}_b)$, which depends on the wall properties [40], is reflected, while the remaining fraction is absorbed by the wall and then immediately re-emitted (under the hypothesis that the walls are saturated) with a temperature that depends only on the material properties, T_b , and velocity distribution χ_{in} given by the Knudsen law

$$\chi_{\text{in}}(\mathbf{x}_b, \mathbf{v}) = \frac{3}{4\pi} \left(\frac{m}{T_b(\mathbf{x}_b)} \right)^2 \cos(\theta) \exp\left(-\frac{mv^2}{2T_b(\mathbf{x}_b)}\right), \quad (23)$$

where θ is the angle between \mathbf{v} and $\hat{\mathbf{n}}$. For T_b we consider an effective temperature that takes into account the energy gain due to Franck–Condon dissociation process [40]. The neutrals are reflected or re-emitted with the same probability as the ions.

The outflowing flux of particles to the wall, Γ_{out} appearing in (22), is the sum of the neutral and ion flux to the wall,

$\Gamma_{\text{out}} = \int_{v_p < 0} |v_p| f_n d^3v + \Gamma_{\text{out},i}$. The ion flux is evaluated considering the contribution of the parallel, $\mathbf{E} \times \mathbf{B}$ and diamagnetic velocities, i.e.

$$\Gamma_{\text{out},i} = - \left(n_i v_{\parallel i} \mathbf{b} + n_i \frac{\mathbf{B} \times \nabla \phi}{B^2} + \frac{\mathbf{B} \times \nabla p_i}{B^2} \right) \cdot \hat{\mathbf{n}}. \quad (24)$$

Assuming that the plasma related quantities (i.e. reaction cross sections and ion flux to the wall) are known, it is possible to express the formal solution of (21) by using the method of characteristics [26]:

$$\begin{aligned} f_n(\mathbf{x}, \mathbf{v}, t) = & \int_0^{r'_b} \left[\frac{S(\mathbf{x}', \mathbf{v}, t')}{v} + \delta(r - r'_b) f_n(\mathbf{x}', \mathbf{v}, t') \right] \\ & \times \exp\left(-\frac{1}{v} \int_0^{r'} \nu_{\text{eff}}(\mathbf{x}'', t'') dr''\right) dr', \end{aligned} \quad (25)$$

where r' is the coordinate along the neutral characteristic defined by $\mathbf{x}' = \mathbf{x} - r' \mathbf{v}/v$, and r'_b is the distance along the characteristic from the position \mathbf{x} and the wall. The effective frequency for neutral removal along the characteristic is $\nu_{\text{eff}} = \nu_{cx} + \nu_{iz}$. The neutral volumetric source is the result of charge–exchange and recombination processes

$$\begin{aligned} S(\mathbf{x}', \mathbf{v}, t') = & \nu_{cx}(\mathbf{x}', t') n_n(\mathbf{x}', t') \Phi_i(\mathbf{x}', \mathbf{v}, t') \\ & + \nu_{rec}(\mathbf{x}', t') f_i(\mathbf{x}', \mathbf{v}, t'), \end{aligned} \quad (26)$$

with $\Phi_i = [m_i/(2\pi T_i)]^{3/2} \exp[-m_i v^2/(2T_i)]$ the ion velocity distribution. In (25) we find an integral equation for f_n that takes into account that neutrals are generated in the plasma volume and at the boundary walls and they are lost along the path from the source to the target positions because of ionization and charge–exchange processes. In fact, \mathbf{x}'' and t'' appearing in (25) indicates the position and time along this path.

As detailed in [26], (25) can be integrated over the velocity space, obtaining an integral equation for the neutral density $n_n(\mathbf{x}, t) = \int f_n(\mathbf{x}, \mathbf{v}, t) d\mathbf{v}$. Under two assumptions, typically valid in SOL conditions, i.e. that the time of flight of neutrals is shorter than the turbulence timescales $\tau_n < \tau_{\text{turb}}$, equivalent to neglect $\partial_t f_n = 0$ in (21), and that the turbulent parallel length scales are longer than neutrals mean free path, $k_{\parallel} \lambda_{\text{mf}} \ll 1$, the following equation for the neutral density is obtained

$$\begin{aligned} n_n(\mathbf{x}_{\perp}) = & \int_D n_n(\mathbf{x}'_{\perp}) \nu_{cx}(\mathbf{x}'_{\perp}) K_{p \rightarrow p}(\mathbf{x}_{\perp}, \mathbf{x}'_{\perp}) dA' \\ & + \int_{\partial D} (1 - \alpha_{\text{refl}}) \Gamma_{\text{out},n}(\mathbf{x}'_{\perp,b}) \\ & \times K_{b \rightarrow p}(\mathbf{x}_{\perp}, \mathbf{x}'_{\perp,b}, T_b) dA'_b \\ & + n_{n[\text{out},i]}(\mathbf{x}_{\perp}) + n_{n[\text{rec}]}(\mathbf{x}_{\perp}), \end{aligned} \quad (27)$$

where D is the poloidal plane that, within the tokamak large aspect ratio approximation, can be considered perpendicular

to \mathbf{B} , ∂D is its boundary, \mathbf{x}_\perp identifies a vector on D and $\mathbf{x}_{\perp b}$ along ∂D . The flux of neutral to the wall $\Gamma_{\text{out}, n}$ is given by

$$\begin{aligned} \Gamma_{\text{out}, n}(\mathbf{x}_{\perp b}) &= \int_D n_n(\mathbf{x}'_\perp) \nu_{cx}(\mathbf{x}'_\perp) K_{p \rightarrow b}(\mathbf{x}_{\perp b}, \mathbf{x}'_\perp) dA' \\ &+ \int_{\partial D} (1 - \alpha_{\text{refl}}) \Gamma_{\text{out}, n}(\mathbf{x}'_{\perp b}) \\ &\times K_{b \rightarrow b}(\mathbf{x}_{\perp b}, \mathbf{x}'_{\perp b}, T_b) da'_b \\ &+ \Gamma_{\text{out}, n[\text{out}, i]}(\mathbf{x}_{\perp b}) + \Gamma_{\text{out}[\text{rec}]}(\mathbf{x}_{\perp b}). \end{aligned} \quad (28)$$

The kernel function $K_{p \rightarrow p}$ represents the probability for a neutral to reach a target point in the plasma volume, p , from a source point also in the plasma. By considering that these two points can be connected directly or through one reflection (we neglect multiple reflections), the following expression is obtained

$$K_{p \rightarrow p}(\mathbf{x}_\perp, \mathbf{x}'_\perp) = K_{p \rightarrow p}^{\text{dir}}(\mathbf{x}_\perp, \mathbf{x}'_\perp) + \alpha_{\text{refl}} K_{p \rightarrow p}^{\text{refl}}(\mathbf{x}_\perp, \mathbf{x}'_\perp), \quad (29)$$

where, for the direct and reflected paths, we have

$$\begin{aligned} K_{p \rightarrow p}^{\text{path}}(\mathbf{x}_\perp, \mathbf{x}'_\perp) &= \int_0^\infty \frac{1}{r'_\perp} \Phi_{\perp i}(\mathbf{x}'_\perp, \mathbf{v}_\perp) \\ &\times \exp \left[-\frac{1}{v_\perp} \int_0^{r'_\perp} \nu_{\text{eff}}(\mathbf{x}''_\perp) dr''_\perp \right] dv_\perp, \end{aligned} \quad (30)$$

having defined path = {dir, refl} and the variable \mathbf{x}''_\perp as the coordinate of a point along the path that connects \mathbf{x}'_\perp and \mathbf{x}_\perp on D . Similarly, the kernel function involving boundary points, b , are defined as

$$\begin{aligned} K_{b \rightarrow p}(\mathbf{x}_\perp, \mathbf{x}'_{\perp b}, T) &= K_{b \rightarrow p}^{\text{dir}}(\mathbf{x}_\perp, \mathbf{x}'_{\perp b}, T) \\ &+ \alpha_{\text{refl}} K_{b \rightarrow p}^{\text{refl}}(\mathbf{x}_\perp, \mathbf{x}'_{\perp b}, T), \end{aligned} \quad (31)$$

$$\begin{aligned} K_{p \rightarrow b}(\mathbf{x}_{\perp b}, \mathbf{x}'_\perp) &= K_{p \rightarrow b}^{\text{dir}}(\mathbf{x}_{\perp b}, \mathbf{x}'_\perp) \\ &+ \alpha_{\text{refl}} K_{p \rightarrow b}^{\text{refl}}(\mathbf{x}_{\perp b}, \mathbf{x}'_\perp), \end{aligned} \quad (32)$$

$$\begin{aligned} K_{b \rightarrow b}(\mathbf{x}_{\perp b}, \mathbf{x}'_{\perp b}, T) &= K_{b \rightarrow b}^{\text{dir}}(\mathbf{x}_{\perp b}, \mathbf{x}'_{\perp b}, T) \\ &+ \alpha_{\text{refl}} K_{b \rightarrow b}^{\text{refl}}(\mathbf{x}_{\perp b}, \mathbf{x}'_{\perp b}, T), \end{aligned} \quad (33)$$

where

$$\begin{aligned} K_{b \rightarrow p}^{\text{path}}(\mathbf{x}_\perp, \mathbf{x}'_{\perp b}, T) &= \int_0^\infty \frac{v_\perp}{r'_\perp} \cos \theta' \chi_{\perp \text{in}}(\mathbf{x}'_{\perp b}, \mathbf{v}_\perp, T) \\ &\times \exp \left[-\frac{1}{v_\perp} \int_0^{r'_\perp} \nu_{\text{eff}}(\mathbf{x}''_\perp) dr''_\perp \right] dv_\perp, \end{aligned} \quad (34)$$

$$\begin{aligned} K_{p \rightarrow b}^{\text{path}}(\mathbf{x}_{\perp b}, \mathbf{x}'_\perp) &= \int_0^\infty \frac{v_\perp}{r'_\perp} \cos \theta \Phi_{\perp i}(\mathbf{x}'_\perp, \mathbf{v}_\perp) \\ &\times \exp \left[-\frac{1}{v_\perp} \int_0^{r'_\perp} \nu_{\text{eff}}(\mathbf{x}''_\perp) dr''_\perp \right] dv_\perp, \end{aligned} \quad (35)$$

$$\begin{aligned} K_{b \rightarrow b}^{\text{path}}(\mathbf{x}_{\perp b}, \mathbf{x}'_{\perp b}, T) &= \int_0^\infty \frac{v_\perp^2}{r'_\perp} \cos \theta \cos \theta' \chi_{\perp \text{in}}(\mathbf{x}'_{\perp b}, \mathbf{v}_\perp, T) \\ &\times \exp \left[-\frac{1}{v_\perp} \int_0^{r'_\perp} \nu_{\text{eff}}(\mathbf{x}''_\perp) dr''_\perp \right] dv_\perp. \end{aligned} \quad (36)$$

The velocity distribution functions appearing in (34)–(36) are integrated over the parallel velocity, that is

$$\Phi_{\perp i}(\mathbf{x}_\perp, \mathbf{v}_\perp) = \int \Phi_i(\mathbf{x}_\perp, \mathbf{v}) dv_\parallel = \frac{m_i}{2\pi T_i} \exp \left(-\frac{m_i v_\perp^2}{2T_i} \right) \quad (37)$$

and

$$\begin{aligned} \chi_{\perp \text{in}}(\mathbf{x}_\perp, \mathbf{v}_\perp, T) &= \int \chi_{\text{in}}(\mathbf{x}_\perp, \mathbf{v}, T) dv_\parallel = \frac{3m_i^2}{4\pi T_i^2} \\ &v_\perp \cos \theta \exp \left(-\frac{m_i v_\perp^2}{4T_i} \right) \mathcal{K}_0 \left(\frac{m_i v_\perp^2}{4T_i} \right) \end{aligned} \quad (38)$$

being $\mathcal{K}_0(x)$ the modified Bessel function of the second kind.

Neutral densities and fluxes due to ion recycling and recombination processes in (27) and (28) do not depend on the neutral density. They are evaluated as

$$\begin{aligned} n_{n[\text{out}, i]}(\mathbf{x}_\perp) &= \int_{\partial D} \Gamma_{\text{out}, i}(\mathbf{x}'_{\perp b}) \\ &\times [(1 - \alpha_{\text{refl}}) K_{b \rightarrow p}(\mathbf{x}_\perp, \mathbf{x}'_{\perp b}, T_b) \\ &+ \alpha_{\text{refl}} K_{b \rightarrow p}(\mathbf{x}_\perp, \mathbf{x}'_{\perp b}, T_i)] da'_b, \end{aligned} \quad (39)$$

$$\begin{aligned} \Gamma_{\text{out}, n[\text{out}, i]}(\mathbf{x}_{\perp b}) &= \int_{\partial D} \Gamma_{\text{out}, i}(\mathbf{x}'_{\perp b}) \\ &\times [(1 - \alpha_{\text{refl}}) K_{b \rightarrow b}(\mathbf{x}_{\perp b}, \mathbf{x}'_{\perp b}, T_b) \\ &+ \alpha_{\text{refl}} K_{b \rightarrow b}(\mathbf{x}_{\perp b}, \mathbf{x}'_{\perp b}, T_i)] da'_b, \end{aligned} \quad (40)$$

$$\begin{aligned} n_{n[\text{rec}]}(\mathbf{x}_\perp) &= \int_D n_i(\mathbf{x}'_\perp) \nu_{\text{rec}}(\mathbf{x}'_\perp) \\ &\times K_{p \rightarrow p}(\mathbf{x}_\perp, \mathbf{x}'_\perp) dA', \end{aligned} \quad (41)$$

$$\begin{aligned} \Gamma_{\text{out}[\text{rec}]}(\mathbf{x}_{\perp b}) &= \int_{\partial D} n_i(\mathbf{x}'_\perp) \nu_{\text{rec}}(\mathbf{x}'_\perp) K_{p \rightarrow b} \\ &\times (\mathbf{x}_{\perp b}, \mathbf{x}'_\perp) dA'. \end{aligned} \quad (42)$$

In order to numerically solve (27) and (28) the poloidal plane is discretized on a uniform (R, Z) grid, and the system is rewritten in matrix form:

$$\begin{pmatrix} n_n \\ \Gamma_{\text{out},n} \end{pmatrix} = \begin{pmatrix} \nu_{\text{cx}} K_{\text{p} \rightarrow \text{p}} & (1 - \alpha_{\text{refl}}) K_{\text{b} \rightarrow \text{p}} \\ \nu_{\text{cx}} K_{\text{p} \rightarrow \text{b}} & (1 - \alpha_{\text{refl}}) K_{\text{b} \rightarrow \text{b}} \end{pmatrix} \begin{pmatrix} n_n \\ \Gamma_{\text{out},n} \end{pmatrix} + \begin{pmatrix} n_{\text{n[out],i}} + n_{\text{n[rec]}} \\ \Gamma_{\text{out}, \text{n[out],i}} + \Gamma_{\text{out[rec]}} \end{pmatrix} \quad (43)$$

The numerical solution of the neutral kinetic equation is finally obtained through the solution of the linear system in (43). Differently with respect to [26], where a region of the core is excluded from the simulation domain, all points in our domain are optically connected also through the reflection on the walls, so all elements in the matrix in (43) are strictly positive. The system is solved by a direct inversion of the matrix using the MUMPS library [46]. Once the neutral density is known as the solution of (43), all moments of the neutral distribution function can be evaluated by considering integrals similar to the one in (27).

3. Overview of the simulation results

The results described in the present work are based on a set of simulations carried out with the GBS code implementing the model described in section 2. All simulations consider the same flux function ψ , which is evaluated from the solution of Biot–Savart law in the infinite aspect-ratio limit for two currents: one centred at the magnetic axis and one outside the domain (see figure 2), as a matter of fact the same equilibrium used in [32]. Contour levels of the flux function are also shown in figure 2. The plasma current on axis is set to have safety factors $q_0 \simeq 1$ at the axis and $q_{95} \simeq 4$ at the edge. In addition, all simulations consider the same geometrical parameters: $L_Z = 800\rho_{s0}$, $L_R = 600\rho_{s0}$, $\rho_*^{-1} = 500$, $a/R_0 = 0.3$. With the choice of $T_{e0} = 20$ eV, if we consider a magnetic field typical of a TCV discharge $B = 0.9$ T and hydrogen species, we find the ion sound speed $c_{s0} = 3.8 \times 10^4$ m s⁻¹, the ion sound Larmor radius $\rho_{s0} = 0.5$ mm, $a = 0.076$ m and $R_0 = 0.254$ m, approximately, 1/3 of the TCV tokamak [38]. Other plasma parameters that are constant throughout the scan are $\tau = 1$, $\tilde{\eta}_{0e} = \tilde{\eta}_{0i} = 1$, $\tilde{\chi}_{\parallel e} = \tilde{\chi}_{\parallel i} = 2$ and $\tilde{D}_f = 16$ for all fields f . In (5) and (6) the temperature source terms are equal for both species $s_{T_e} = s_{T_i} = s_T$, where s_T is toroidally uniform and we express it as an analytical function of the flux function

$$s_T = \frac{s_{T0}}{2} \left[\tanh \left(-\frac{\psi(R, Z) - \psi_T}{\Delta_T} \right) + 1 \right], \quad (44)$$

where ψ_T is a flux surface localized inside the LCFS, at a position $R - R_{\text{sep}} = -45\rho_{s0}$ at $Z = 0$, as shown in figure 2, and Δ_T corresponds to an interval $\Delta R = 40\rho_{s0}$ at $Z = 0$.

Regarding the parameters that describe the neutral–plasma interaction, we consider an effective ionization energy of $E_{iz} =$

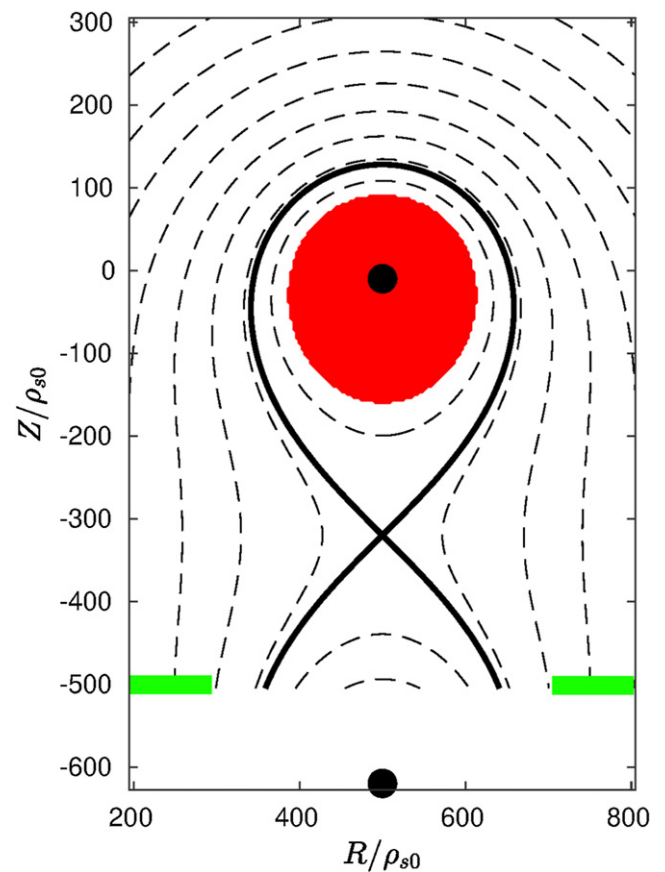


Figure 2. Flux surface of ψ function in the domain considered for our simulations. The two black dots represent the position of the current density that generates the magnetic field. The bottom dot is outside the simulation domain. The red region indicate the position of the temperature source, the green lines indicate the pumping regions at the lower boundary of the domain.

30.0 eV, taking into account the radiation losses that occur with ionization [40]. Volumetric recombinations and recycling on the left and right walls are neglected, while for all four walls a constant reflection coefficient $\alpha_{\text{refl}} = 0.2$ is considered. Taking into account the energy associated with Franck–Condon dissociation processes, the emission temperature of the neutrals is set to $T_b = 3$ eV [40]. At the bottom-left and bottom-right corners of the rectangular poloidal plane we introduce two neutral pumping regions where neutral emission is suppressed (green line in figure 2). In addition, to avoid that the density in the private flux region drops to very low values that are detrimental for the numerical stability of the simulations, we use a gas puff that provides a small source of neutrals in this region. This source, which has the same amplitude in all simulations, does not have a relevant impact on the simulation results.

In the scan we control the neutral reaction rates by varying the normalized plasma resistivity ν_0 (see (9)). Then, to have simulations in comparable conditions, the amplitude of the temperature source s_{T0} is adjusted to have the same power outflowing into the SOL for all the three simulations (we choose the value $S_p \simeq (313 \pm 34)$ kW). The parameters that are varied throughout the simulations are summarized in table 1, with the density values being normalized to the same

$n_0 = 4 \times 10^{-19} \text{ m}^{-3}$. Since simulations with higher ν_0 show higher fuelling in the core (S_n defined in (11)), in the following we name the simulations with low, medium and high fuelling as $S_{n,l}$, $S_{n,m}$ and $S_{n,h}$. As discussed later, we compare our simulations with the results of a set of simulations that do not include neutral dynamics, similar to those described in [32], and have the same power source S_P as the simulations with neutrals and same density source, $S_{n,l}$, $S_{n,m}$ and $S_{n,h}$.

We use a grid $N_R \times N_Z \times N_\phi = 240 \times 320 \times 80$ and a time-step $\Delta t = 3 \times 10^{-5} t_0$ to discretize the plasma equations. The grid for the neutrals is $N_R^n \times N_Z^n \times N_\phi^n = 72 \times 96 \times 80$ and the solution of the neutral model is evaluated every $\Delta t \simeq 0.1 t_0$. The grid used and the neutrals evaluation frequency ensure that our simulation results are converged [28].

After a transient the simulations reach a quasi-steady state where plasma and neutral quantities oscillate around a constant value. In these conditions, the sources, parallel and perpendicular transport and the losses at vessel balance each other. We remark that the parameter chosen for our simulations mimic the typical conditions found in L-mode diverted discharges, as described in [32]. In this regime, turbulent transport is mostly interchange dominated and is characterized by eddies developing near the separatrix, with small or negligible effects due to $E \times B$ shear.

Typical simulations results during this quasi-steady state are shown in figures 3 and 4. All quantities are averaged toroidally and over a $15 t_0$ period (we will denote with tilde fluctuating quantities and with the overline their time average, e.g. $\phi = \tilde{\phi} + \bar{\phi}$). The neutral density, flux and temperature in the poloidal plane are shown in figure 3 (the $S_{n,l}$ simulation is considered). Neutral density peaks at the bottom wall, near the strike points where most of the ions impact the wall and are recycled. The presence of neutrals is observed both in the private and common flux regions. The neutral flux is large near the divertor plates and points towards the core, rapidly decreasing because of the loss of neutrals due to ionizations and the effect of charge-exchange collisions on the neutral velocity. Inside the LCFS, above the X-point, plasma temperature and density are sufficiently high to ionize the remaining neutrals. Neutral temperature is lower at the target walls, where most of the neutrals are created, and has a value close to $T_b = 3 \text{ eV}$. The temperature increases inside the plasma volume because of charge-exchange reactions, which produce high temperature neutrals. The average plasma density, electron and ion temperatures, the average plasma parallel current and the average electrostatic potential, are shown in figure 4. These profile are in qualitative agreement with past GBS simulations without neutrals [32, 39], suggesting that the density source used in the simulations without neutral dynamics is able to mimic the self-consistent fuelling that takes place as a consequence of the plasma-neutrals interactions.

The simulations with higher S_n are expected to have, in general, higher reaction rates for the collisions between plasma and neutral particles, through the enhancement of the neutral

interaction terms in (1)–(6), affecting therefore the simulation results. In fact, higher density source S_n is the result of higher ionization reaction rates, which introduces a temperature sink lowering the temperature in the core and in the SOL, despite the fact that the amplitude of the temperature source, s_{T0} , is increased to keep the power constant throughout the scan. In particular, this leads to an increase in resistivity at the separatrix, $\nu_{\text{sep}} \propto T_{e,\text{sep}}^{-3/2}$ (see table 1).

In the present work we focus on the profiles of plasma density and electron pressure at the OMP, where for OMP we consider the average over a region of vertical extension $20 \rho_{s0}$. In figure 5 the density and electron pressure profiles are shown for the three simulations considered. The fits of the density and electron pressure reveal two different decay lengths. A steep decay is observed in the near SOL and across the LCFS. We indicate the density and pressure decay lengths in this region as L_n^{near} and $L_{p_e}^{\text{near}}$. A weaker decay is observed further away from the separatrix, in the far SOL, denoted L_n^{far} and $L_{p_e}^{\text{far}}$. This double decay length is a feature seen both in experiments [9, 48] and simulations [49]. One also observes that the density increases in the far SOL with increasing core fuelling S_n , a property that recalls the formation of the density shoulder seen experimentally [11, 50].

In order to quantify the double scale length structure and its dependence on S_n , we introduce the separatrix density, n_{sep} , and temperature, $T_{e,\text{sep}}$ and define the transition density n_{tr} as the density at the intersection between the exponential fits of the near and far SOL density profile. We also introduce the ratio of the density at the interface between far and near SOL expressed as $\theta = n_{\text{tr}}/n_{\text{sep}}$. When $\theta \simeq 1$ the profile exhibits high density in the far SOL, without a clear separation between near and far SOL. Table 1 provides the computed values for all simulations.

Besides the mentioned increase in resistivity at the separatrix, the analysis of the simulation results at the OMP shows that the increase of S_n leads to the increase of θ , and therefore of the far SOL density. Higher fuelling is also associated with a less noticeable increase of L_n^{near} . The increase of the far SOL density and L_n^{near} with ν_{sep} is a feature already observed with GBS [32], but in our simulations the increase in resistivity is the self-consistent result of the increase of neutral ionizations. The far SOL decay length, L_n^{far} , instead shows differences below 15%, suggesting comparable perpendicular flux far from the separatrix, expected to be proportional to the L_n^{far} [39].

The behaviour of the decay lengths both in near and far SOL has been subject of previous investigations in similar configurations without neutrals [39]. The simulation results are in good agreement with the analytical estimate in [39], based on the separatrix values of the plasma temperature and resistivity, as well as the power coming from the core into the SOL. This result suggests that the presence of neutrals do not affect the validity of the estimate L_n^{near} , $L_{p_e}^{\text{near}}$, L_n^{far} and $L_{p_e}^{\text{far}}$ and therefore the underlying transport mechanisms, but they rather modify the separatrix values of plasma temperature and density.

Table 1. Input parameters, ν_0 and s_{T0} , and main results of the three simulations considered in the present paper. All simulations have the same core power source, $S_p \simeq (313 \pm 34)$ kW, while the density source in the core, S_n , is given by ionization reactions. Density values and sources are normalized to the same reference density $n_0 = 4 \times 10^{19} \text{ m}^{-3}$, temperatures to the reference electron temperature $T_{e0} = 20 \text{ eV}$.

| Label | ν_0 | $s_{T0}/(T_{e0}/t_0)$ | $S_n/(n_0 \rho_{s0}^2/t_0)$ | n_{sep}/n_0 | $T_{e,\text{sep}}/T_{e0}$ | θ | ν_{sep} | $L_n^{\text{near}}/\rho_{s0}$ | $L_n^{\text{far}}/\rho_{s0}$ |
|-----------|---------|-----------------------|-----------------------------|----------------------|---------------------------|----------|--------------------|-------------------------------|------------------------------|
| $S_{n,l}$ | 0.4 | 0.16 | 0.97×10^3 | 0.47 | 1.16 | 0.74 | 0.81 | 25.89 | 186.34 |
| $S_{n,m}$ | 0.8 | 0.20 | 1.10×10^3 | 0.53 | 0.97 | 0.86 | 1.05 | 35.66 | 189.42 |
| $S_{n,h}$ | 1.6 | 0.22 | 1.35×10^3 | 0.55 | 0.86 | 0.90 | 1.26 | 65.26 | 205.27 |

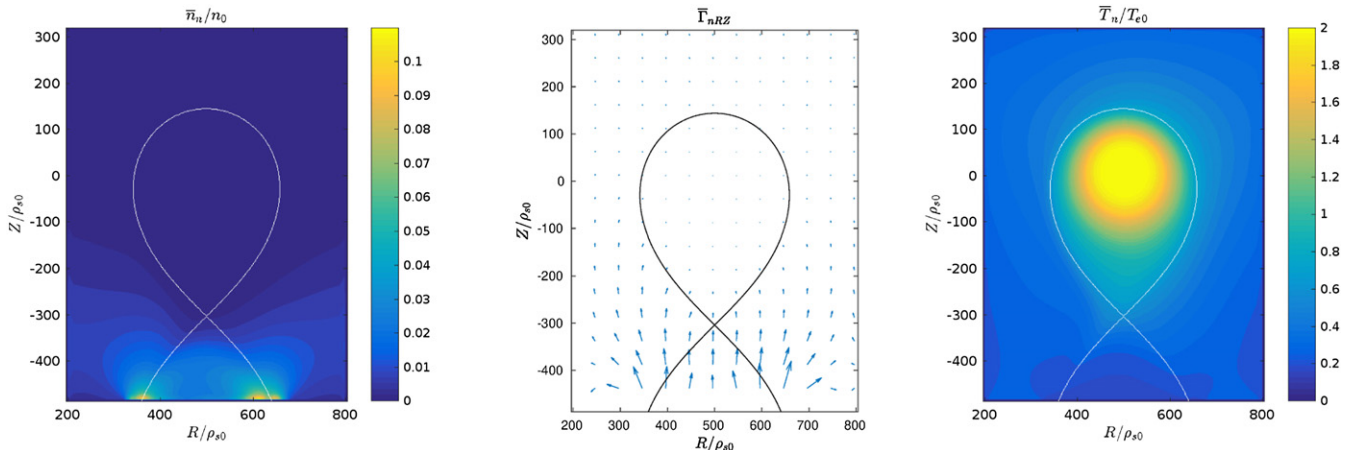


Figure 3. Time and toroidally averaged neutral density, \bar{n}_n/n_0 , neutral flux, $\bar{\Gamma}_{n,RZ}$, and neutral temperature, \bar{T}_n/T_{e0} , for the $S_{n,l}$ simulation.

4. Investigation of the mechanisms behind the density shoulder formation

The plasma profiles in the SOL are the results of the interplay between perpendicular transport of plasma and heat from the core towards the wall, transport along the magnetic field lines to the divertor plates and local interactions with the neutral species.

Enhanced perpendicular transport due to large filaments is currently thought to be one of the main causes for shoulder formation [7, 11, 51]. Along with this mechanism, two other effects were proposed to have a significant impact in the broadening of the SOL profiles, that is the decrease in parallel transport [10, 52] and the increase in ionization in the OMP [6, 9, 12]. In the following we disentangle the three effects in order to investigate the mechanisms behind the shoulder formation.

While we focus on the density profiles and fluxes in what follows, we note that the flattening of pressure profile is also shown as S_n is increased (see figure 5). This is despite the fact that the increase of ionizations with S_n is responsible for the decrease of the electron temperature at the separatrix.

4.1. Perpendicular transport

We focus on $\bar{\Gamma}_{E \times B}$, the time and toroidally averaged cross-field transport induced by the $E \times B$ drift, since it is significantly larger than the one induced by the diamagnetic drift. In addition, we observe that the contribution of the stationary flow $\bar{n} \partial_\chi \bar{\phi}$ to $\bar{\Gamma}_{E \times B}$ can be neglected, consistently with

the general observation that perpendicular transport is mostly driven by turbulence. It is therefore possible to approximate $\bar{\Gamma}_{E \times B} \simeq \bar{n} \partial_\chi \bar{\phi}$.

In figure 6 we show the radial profiles of $\bar{\Gamma}_{E \times B}$, $\bar{\Gamma}_{E \times B}/|\nabla \bar{n}|$ and $\bar{\Gamma}_{E \times B}/\bar{n}$ at the OMP for the three simulations. We observe that the average of all quantities decrease progressively with the increase of S_n and, therefore, with the plasma resistivity, as opposed to the increase of \bar{n} in the far SOL. In particular, $\bar{\Gamma}_{E \times B}/|\nabla \bar{n}|$ shows that the effective plasma turbulent diffusion coefficient in the far SOL decreases with the increase of S_n . The same result are retrieved from the profile of $\bar{\Gamma}_{E \times B}/\bar{n}$, an estimate of the effective convective transport velocity, that decreases with increasing ionization source. This contrasts, at least in the condition explored in the present set of simulations, with the hypothesis advanced since the first experimental evidences [53, 54], that shoulder formation is due to an enhanced perpendicular transport. As an aside, we note that the diffusivity parameters D_f introduced for numerical stability are one order of magnitude lower than the turbulent transport coefficient shown in figure 6.

In order to investigate the reason behind the decrease of the transport with S_n , we carry out a detailed investigations of the mechanisms that determine it. Our simulations as well as experimental evidences, show that transport in the far SOL is highly intermittent and associated with the radial motion of coherent filamentary structures denoted as blobs [11, 51, 55–57]. In our simulations, blobs are identified and their motion is studied with an algorithm developed and used for the analysis of previous GBS results [42, 58, 59]. The

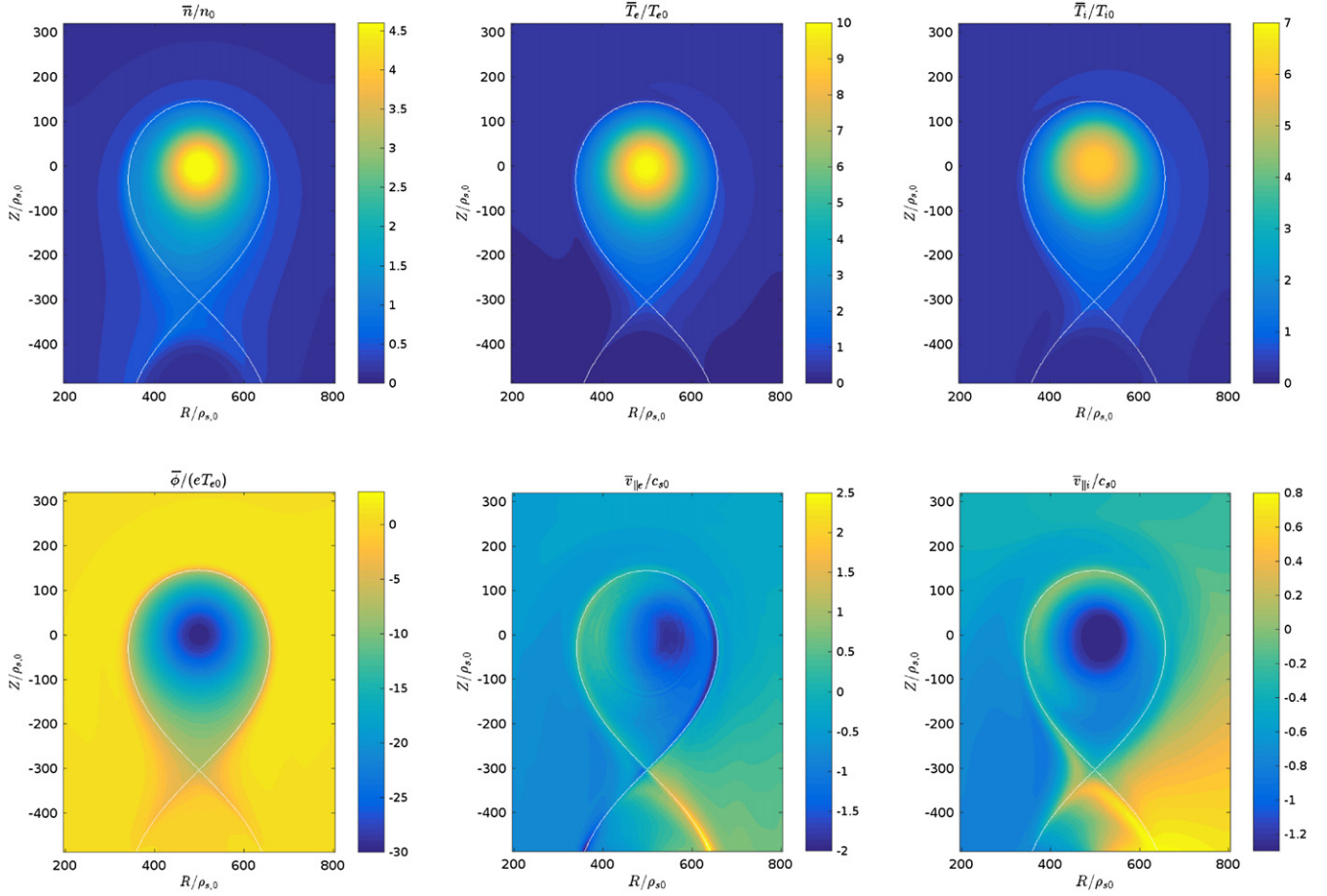


Figure 4. Time and toroidally averaged plasma density, \bar{n}/n_0 , electron temperature, \bar{T}_e/T_{e0} , ion temperature, \bar{T}_i/T_{e0} , electrostatic potential, $\bar{\phi}/(eT_{e0})$, electron parallel velocity, $\bar{v}_{||e}/c_{s0}$, and ion parallel velocity, $\bar{v}_{||i}/c_{s0}$, for the $S_{n,1}$ simulation.

algorithm detects the region where the density fluctuations are 2.5 times above the local standard deviation and tracks them in time. If the fluctuations are detected as coherent, they are identified as a blob. The density perturbation associated with each blob is then fitted with a Gaussian function that has full width at half maximum, a_{Ri} and a_{Zi} , in the radial and vertical direction (i is the blob index), amplitude n_{bi} and radial velocity v_{bi} . The radial transport due to the blobs is then evaluated as the sum of the contribution of all blobs

$$\Gamma_b(R, Z) = \sum_i n_{bi} v_{bi} \exp \left[-\frac{(R - R_i)^2}{2a_{Ri}^2} - \frac{(Z - Z_i)^2}{2a_{Zi}^2} \right], \quad (45)$$

where (R_i, Z_i) are the coordinates of the centre of mass of the i th blob. From the blobs centre of mass motion it is also possible to retrieve the average blob velocities in the poloidal plane, $v_{b,\psi}(R, Z)$ and $v_{b,\chi}(R, Z)$. Our analysis considers all the blobs tracked in the low-field side above the X-point, ensuring statistical convergence to proceed with the detailed study of the $\Gamma_{E \times B}$ flux.

In our simulations, blob transport contribute to about half of the transport in the far SOL [58]. In addition, similarly to [39], blobs are in the RX or RB regimes (i.e. the charge separation inside the fluctuation is damped by parallel resistivity or by the ion polarization current due to the fanning of the

flux surfaces [59, 60]), with good agreement between the blob velocity measured in the simulations and the analytical scaling. Thus, we find that the results of the blob tracking analysis are in agreement with the results of previous investigations where the neutral dynamics was not considered.

The histograms for blob size and radial velocity, resulting from the blob tracking algorithm, are shown in figure 7 separating the near and far SOL. The size is evaluated as the arithmetic average between the radial and poloidal width, which are similar in most cases [42, 59], and the radial velocity as the time-averaged velocity of a blob while the blob is in the region of interest. We first observe that the average blob size increases with S_n both in near and far SOL, leading to a small increase of the average packing fraction from 4% to 4.6%. This is due to a strong decrease of the number of small size blobs, and an increase of the number of larger blobs. The increase of blob size for increasing resistivity is a result well known from previous simulations [42], thus hinting that the effect provided by the addition of neutrals is linked to the change in plasma resistivity. On the other hand, our simulations point out a decrease of the blob velocity with S_n in the far SOL, due to an increase in the number of slow blobs. We note that ionization processes reduces the electron temperature at high S_n . As we discuss in section 4.3 the reduction of the plasma and the blob temperature lowers the radial blob velocity as a consequence of the

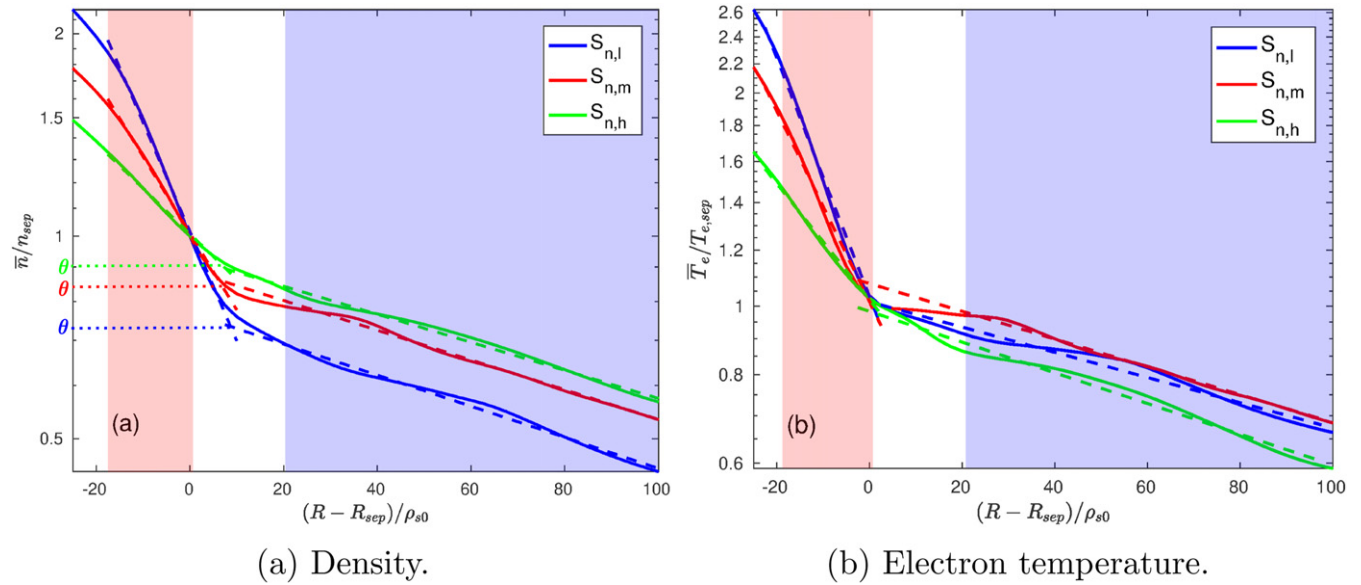


Figure 5. Averaged radial profile of density (a) and electron temperature (b) normalized to the value at the separatrix at the OMP. Dashed line represent the exponential fit in the near SOL and in the far SOL. In red shadow the region used for the near SOL fit, in blue the region for the far SOL fit. Pointed line represent the value of $\theta = n_{tr}/n_{sep}$.

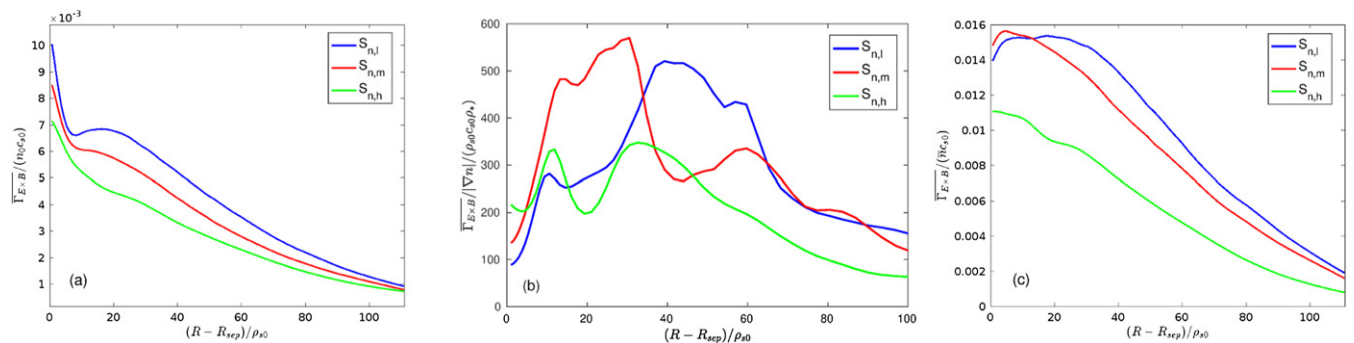


Figure 6. Radial profile of perpendicular transport $\bar{\Gamma}_{E \times B}$ (a), $\bar{\Gamma}_{E \times B}/|\nabla n|$ (b) and $\bar{\Gamma}_{E \times B}/\bar{n}$ (c) at the OMP. All profiles are normalized to their reference value.

reduction of the interchange drive [59]. This conclusion is supported by the analysis of the set of simulations with the same power source S_P and density source $S_{n,l}$, $S_{n,m}$ and $S_{n,h}$, that do not include the interaction with neutrals. In fact in simulations without neutrals both the radial velocity and the size of the blobs are observed to increase with ν [32, 42, 59], supporting the idea that the velocity decrease observed with neutrals is indeed due to the presence of neutral interactions. We note that the effect of neutral interactions on blob velocity is discussed in [6], showing a decrease in radial velocity when compared to results without neutrals and with an increase in background density, in agreement with our result.

Experimental evidence hints towards a correlation between blob size and density decay length, which is observed to increase with the edge Greenwald fraction, i.e. the edge density normalized to Greenwald density [11]. In our simulations, the increase in L_n^{near} is in fact correlated with the increase of the blob size, showing a promising agreement with experiments. However, in our simulations larger structures do not

correspond to higher turbulent fluxes in the far SOL, as it was hypothesized [9], due to the decrease of the blob velocity. Experimentally, the relation between blobs radial velocity and edge density was investigated in several devices, but with no conclusive results, showing for example weak proportionality in AUG [51, 61] or inverse proportionality in TCV [7, 11, 62]. The results of our simulations agree with experimental observations, although a detailed comparison should be made to reduce the differences between simulation and experimental setup (e.g. considering a realistic magnetic configuration).

To conclude, our simulations show a decrease of $\Gamma_{E \times B}$ with S_n in the far SOL, due to a reduced blob velocity, despite the larger size of the blobs. As a consequence, the formation of the density shoulder observed in our simulations is not related to an increase of the perpendicular turbulent transport, as proposed from the interpretation of experimental results [9]. Our result is also different from other modelling studies [12], where the density shoulder is obtained through an increase of radial

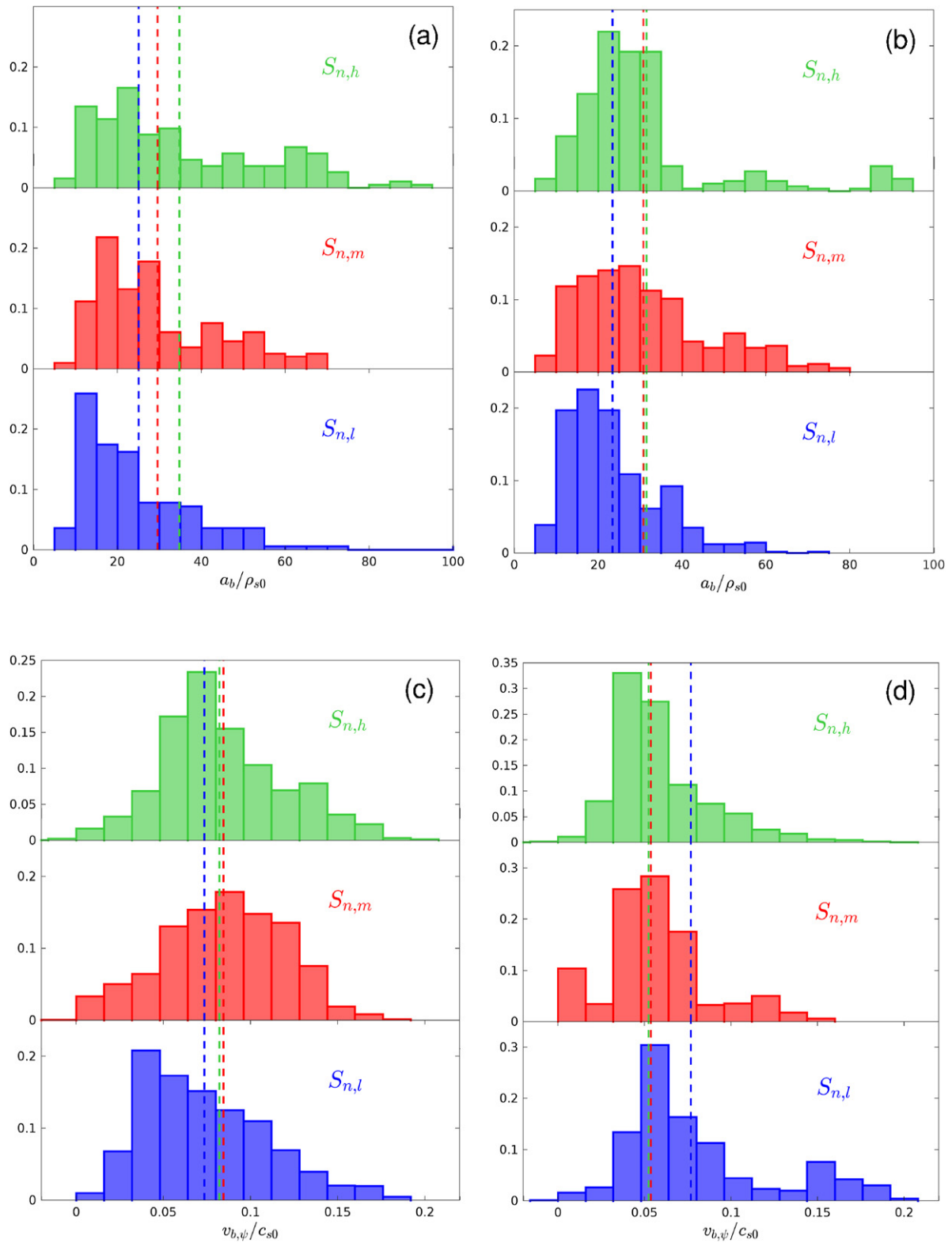


Figure 7. Histograms of the blob size for the simulations listed in table 1 for near SOL, $R_i - R_{\text{sep}} \in [0, 20]\rho_{s0}$ (a) and far SOL, $R_i - R_{\text{sep}} > 20\rho_{s0}$ (b) and histograms of blob centre of mass radial velocity for near (c) and far (d) SOL. The dashed line represents the average value for each quantity and the colour is representative of the considered simulation.

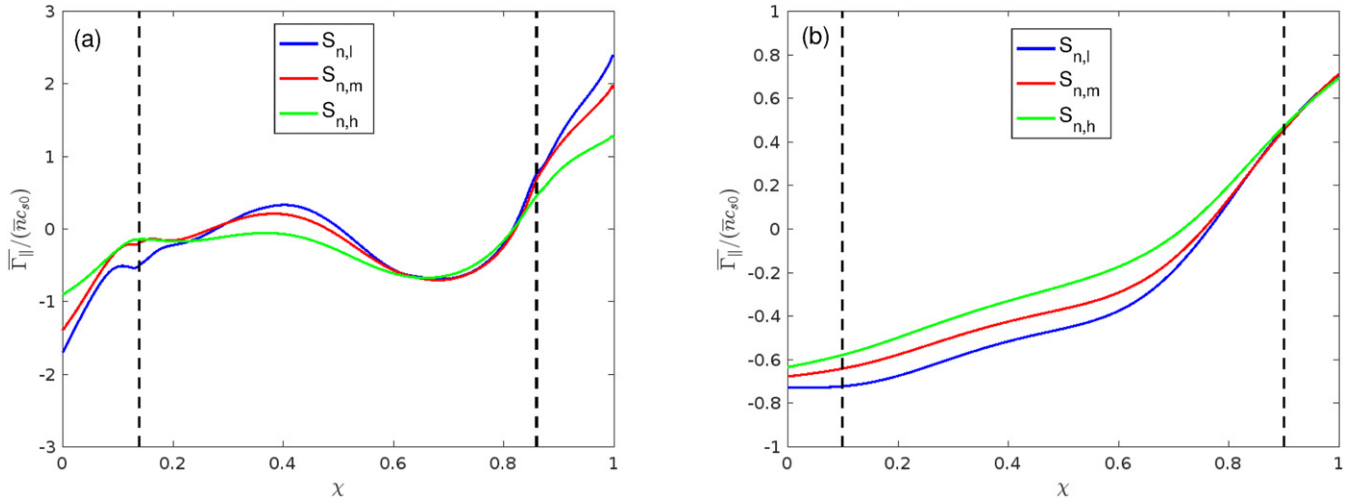


Figure 8. Averaged parallel transport profiles along $\nabla\chi$ in a flux tube of width $= 7\rho_{s0}$, in the near SOL, $R - R_{\text{sep}} = 4\rho_{s0}$ (a), and in the far SOL, $R - R_{\text{sep}} = 70\rho_{s0}$ (b). The black dashed lines indicate the position of the X-point.

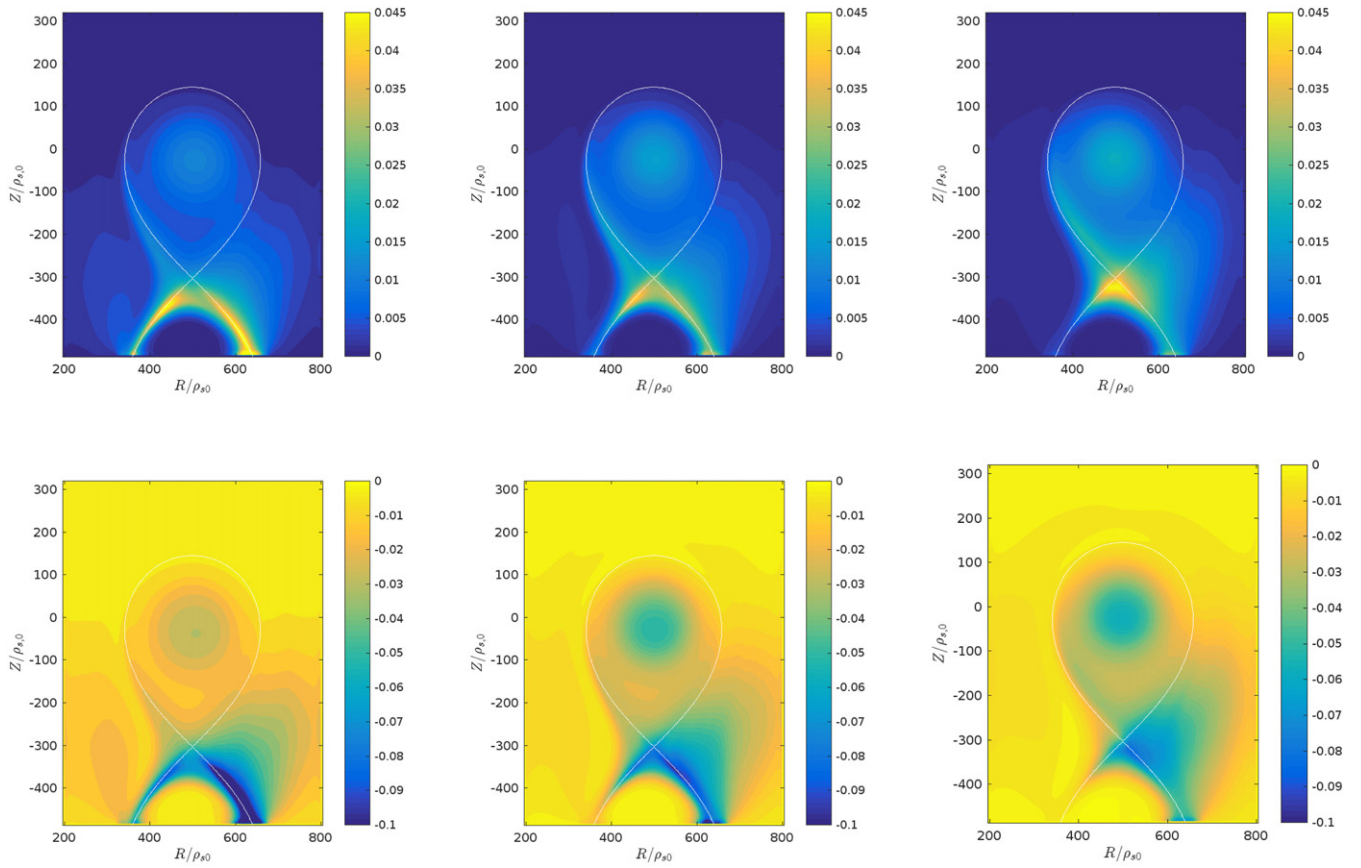


Figure 9. Averaged ionization density source, s_n^n (top) and electron temperature neutral interaction term $s_{T_e}^n$ (bottom), normalized to their reference values. From the left to the right columns the $S_{n,l}$, $S_{n,m}$ and $S_{n,h}$ simulations are considered.

transport, without changes in the ratio $\Gamma_{\perp}/\Gamma_{\parallel}$. In fact, as we show in the analysis of the parallel transport terms, larger S_n is responsible for the reduction of both parallel losses and perpendicular transport. However parallel flux is significantly

more affected than the perpendicular transport, increasing the ratio $\Gamma_{\perp}/\Gamma_{\parallel}$. Ultimately, in our simulations the decrease of parallel flux affects plasma density profile more than the changes in the perpendicular flux.

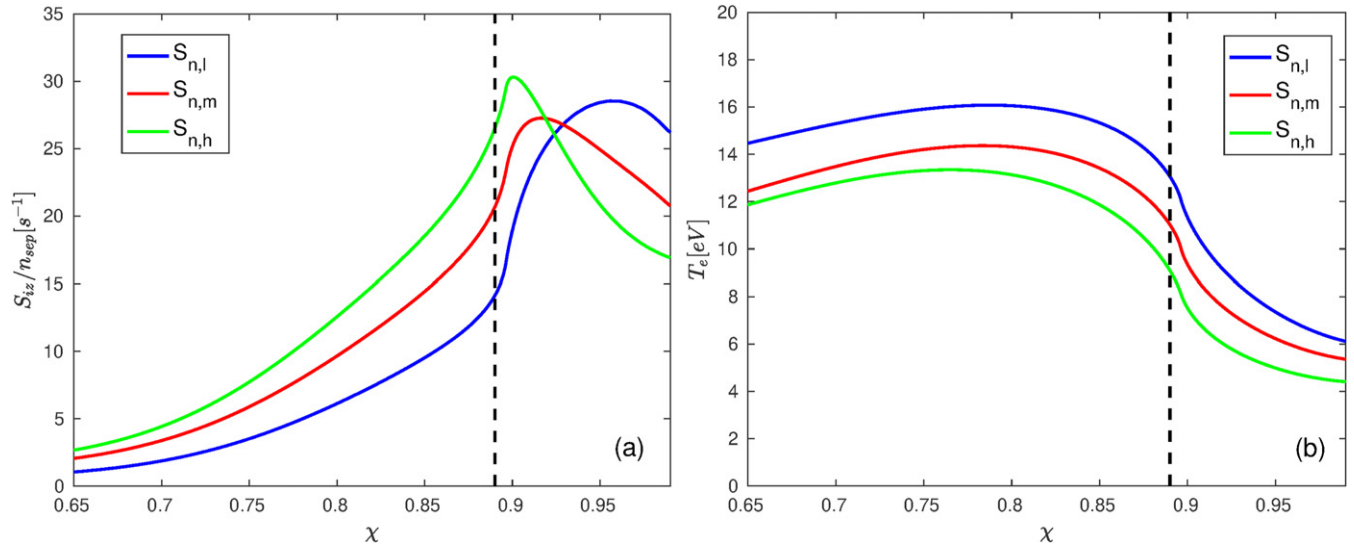


Figure 10. Averaged ionization source (a) and temperature profile outside the LCFS (b), in physical units (for an easier evaluation of the cross sections). Quantities are averaged in time, along the toroidal direction and in the radial direction throughout the SOL. The poloidal coordinate is normalized so that $\chi = 0$ at the left strike point, and $\chi = 1$ at the right strike point. In black dashed line the coordinate of the X-point.

4.2. Parallel transport

Parallel transport appears on the right-hand side of (1) as the divergence of the parallel density flux $\Gamma_{\parallel} = nv_{\parallel e}$. In contrast to the perpendicular transport, fluctuations are subdominant in determining the parallel transport, which can therefore be estimated as $\bar{\Gamma}_{\parallel} \simeq \bar{n}\bar{v}_e$.

In figure 8 we show $\bar{\Gamma}_{\parallel}/\bar{n}$ along two magnetic field lines located at two different radial distances from the LCFS, indicative of the behaviour in the near and far SOL. The χ coordinate along the magnetic field line is normalised so that $\chi = 0$ represents the high-field side strike point and $\chi = 1$ the low-field side one, whereas the OMP is around $\chi \simeq 0.65$. The dashed vertical lines indicate the χ coordinate at the height of the X-point.

We start our analysis from the near SOL. In the divertor region, the modulus of the plasma velocity increases towards the targets where it reaches the local sound speed, $c_s = \sqrt{T_e/m_i}$. As shown in section 4.3, ionization processes lower the electron temperature at large S_n , reducing the parallel velocity at the strike points. However, parallel transport is in general small in the upstream region near the separatrix ($0.2 < \chi < 0.8$), with the presence of two stagnation points that are not significantly affected by S_n . In contrast to the near SOL, a strong difference is observed in the parallel flux at the OMP, $\chi \in [0.65, 0.75]$ in the far SOL. In fact, the parallel flow decreases from the lower to the higher S_n simulation by, approximately, 50%. This results from a decrease of the particle velocity at the inner target in the far SOL, while there is no significant variations at the outer target throughout the simulation scan considered here.

We can then conclude that at large value of S_n , a low parallel transport is observed at the OMP in the far SOL. Interestingly this decrease of parallel transport occurs at the radial distance $R - R_{\text{sep}} > 20\rho_{s0}$, which corresponds to the location where,

as shown in figure 5, we observe the increase of plasma density. This is a result already observed in L-mode experiments, revealing that the Mach number is lower in discharges with higher divertor collisionality [13].

The same analysis carried out for simulations without neutrals supports these results, showing that parallel transport decreases with increasing density source in the core, because higher density source and same input power leads to lower temperature and, consequently, to lower velocities. However, the decrease is stronger when accounting for neutral interactions, where the ionization reactions act as a sink of T_e also in the SOL, further reducing the parallel velocity and the parallel losses.

The analysis of perpendicular and parallel flux gives the possibility to describe the flattening of density profile in terms of the increasing ratio $\Gamma_{\perp}/\Gamma_{\parallel}$. In the near SOL this ratio is approximately independent of S_n , $\Gamma_{\perp}/\Gamma_{\parallel} = 0.021 \pm 0.002$ while, in the far SOL, it increases from a value of $\Gamma_{\perp}/\Gamma_{\parallel} = 0.029$, for the lowest S_n , to $\Gamma_{\perp}/\Gamma_{\parallel} = 0.043$, for the highest S_n . This result confirms that the ratio $\Gamma_{\perp}/\Gamma_{\parallel}$ is important in the shoulder formation, as suggested in [13, 53, 54]. In addition, our analysis shows that this is mostly due to the decrease of parallel transport in the far SOL due to the electron cooling observed at highest values of S_n .

4.3. Ionization and interaction with neutrals

Neutral interactions enter directly on the right-hand side of (1) through the ionization source term, proportional to the neutral density and to the ionization frequency. With the increase of S_n , one observes an increase of the ionization rate in the SOL region (see figure 9). However, the comparison of the local ionization term with the other terms in (1) and, in particular, with the divergence of the parallel flux $\nabla_{\parallel}\Gamma_{\parallel}$, shows that the contribution of the local ionization to the density balance at the

OMP is negligible. This points out that in our simulations the local source of plasma particle does not play a relevant role in the density shoulder formation, as proposed in other modelling studies [9, 12]. On the other hand, ionization events play a role in the increase of the far SOL density by reducing parallel losses.

We first note that the localization of the ionization source depends on S_n , as shown in figure 9. At the lowest S_n , the ionization front is localized along the divertor leg, where the density source and temperature sink are most important (see the left column in figure 9). As S_n increases, ionization events become more important at the X -point, at the OMP and in the core (see the right column in figure 9). The low temperature reached below the X -point explains the shift of the ionization front towards the midplane with increasing S_n . Figure 10 shows the average s_n^n and T_e in the SOL, as a function of the coordinate parallel to the magnetic field χ . We note a decrease of the ionization density source for $T_e < 8$ eV, a threshold below which the ionization rate decreases rapidly, as shown in figure 1. In addition, the integral of the temperature sink due to ionization reactions in the core, $S_{T_e}^n$, increases (in absolute value) with S_n , and the temperature sink of the $S_{n,h}$ simulation is larger than the one of the $S_{n,l}$ simulation by 50%. Despite the fact that the amplitude of the temperature source, s_{T_0} , is adjusted to have the same S_p in all the simulations (see table 1), the increase of ionization reactions above the X -point is responsible for a reduction of T_e in all the SOL region with the increase of S_n .

Our results are in agreement with recent experimental observations that hint to the importance of high neutral density in the main chamber of tokamaks as a necessary condition to observe the density shoulder [63]. In fact all neutrals emitted near the target can reach the plasma volume in our system, similarly to an open divertor configuration. Therefore, the increased fuelling corresponds to an increase of ionization reactions above the X -point, both inside and outside the LCFS. The increase of S_n reduces the plasma temperature, in the core and SOL region. The lower temperature leads to a reduced parallel velocity, which is ultimately responsible of the density shoulder formation.

5. Conclusions

In this work we present the first self-consistent GBS simulations of the plasma turbulence and single-species kinetic neutral dynamics in a diverted configuration. We leverage the new capability of GBS to simulate the interplay between plasma and neutrals in arbitrary magnetic configurations and run simulations in steady state with a self-consistent treatment of the particle source as they result from the interaction with the neutrals.

We present results obtained from three different simulations at different core fuelling. The simulations are carried out with a relatively simple model for the interaction of the plasma with the neutrals that includes only ionization, elastic collisions, recombination and charge exchange. However, despite this simplicity, our simulations are able to retrieve some of the

most important features associated with the increase of neutral density. For example, an increase in neutral density in the divertor region corresponds to a shift of the ionization peak from the bottom wall to the X -point, as shown in figure 9. The position of this peak is set by the balance between the drop of T_e due to ionization reactions and the increase of the ionization cross section with T_e .

We observe that the increase in fuelling source causes a reduction of electron temperature, higher resistivity at the LCFS and higher densities in the far SOL. By considering particle balance in the SOL we observe that within the simulated scenarios the higher density is ultimately caused by a reduction of parallel flux due to the lower temperature at the target. Changes in the ionization and perpendicular fluxes have a lower impact on the OMP density, the first one increasing with increasing density, the second one decreasing. Leveraging methods developed in past studies [39, 42, 52], we perform a detailed investigation of the filamentary transport in the far SOL. When neutral interactions are considered, we observe an increase of the blob-size at higher density source and resistivity, whereas the average blob radial velocity decreases in the far SOL. These results are compatible with recent 2D blob-simulations [6] which showed a slowing down of the centre of mass velocity at increased background plasma and neutral density. The mechanisms described by our simulations, where density shoulder is the consequence of reduced parallel transport, seems different from the one observed through diffusive transport models, with density shoulder being obtained by an increase of the perpendicular diffusion coefficient and both perpendicular and parallel fluxes grow [12].

The simulations exhibit the same variation of the near-SOL e-folding length with collisionality that is observed in simulations without neutrals. Such an estimate is compatible with the interpretation suggested in [32] assuming a weak effect of the $E \times B$ shear. On the other hand, it is worth noting that the presence of neutrals could profoundly change the radial electric field pattern [43, 64, 65] at the separatrix and this will be subject of future investigation. The far SOL scale lengths are observed to be weakly affected by the density source intensity.

Compared with experimental observations, several qualitative similarities may be drawn. As in the experiments, whenever fuelling S_n is increased, our simulations are able to reproduce the increased e-folding length in the near SOL as well as the increase of the blob size. Nevertheless through a detailed analysis of the different transport contributions we are able to associate the increased SOL density to a reduction of the parallel flux, caused by a drop of the temperature because of the increased neutral interactions. The drop in parallel flux is a result seen in experiments [13, 63], but its importance in the density shoulder formation is still under debate [10].




The present analysis constitute a first step in the study of the density shoulder formation with simulations that couple plasma turbulence and the self-consistent kinetic neutral dynamics. In the future, simulations with a more realistic magnetic geometry will be considered, together with the possible contribution of neutrals coming not only from the divertor region but also from vessel wall recycling. Neutrals interaction will be further developed including molecular reactions,

which may play an important role when approaching detached divertor condition, as well as the presence of impurities that might affect the power losses through radiations terms.

Acknowledgements

The simulations presented herein were partially carried out on the CINECA Marconi supercomputer under the neutralGBS project, partially at the Swiss National Supercomputing Centre (CSCS) under the Project IDs s882 and s1028 and partially at SuperMUC-NG thanks to a PRACE awards. This work, supported in part by the Swiss National Science Foundation, has been carried out within the framework of the EUROfusion Consortium and has received funding from the Euratom research and training programme 2014–2018 and 2019–2020 under Grant Agreement No. 633053. The views and opinions expressed herein do not necessarily reflect those of the European Commission.

ORCID iDs

N. Vianello  <https://orcid.org/0000-0003-4401-5346>
 M. Giacomin  <https://orcid.org/0000-0003-2821-2008>
 A. Coroado  <https://orcid.org/0000-0001-9619-4265>

References

- [1] Stangeby P.C. 2018 *Plasma Phys. Control. Fusion* **60** 044022
- [2] Stangeby P. 2020 *Plasma Phys. Control. Fusion* **62** 025012
- [3] Stangeby P. 2020 *Plasma Phys. Control. Fusion* **62** 025013
- [4] D'Ippolito D.A. and Myra J.R. 2002 *Phys. Plasmas* **10** 4029
- [5] Zhang Y. and Krasheninnikov S.I. 2020 *Plasma Phys. Control. Fusion* **62** 115018
- [6] Thrysøe A.S., Naulin V., Nielsen A.H. and Rasmussen J. 2020 *Phys. Plasmas* **27** 052302
- [7] Vianello N. et al 2017 *Nucl. Fusion* **57** 116014
- [8] Militello F., Garzotti L., Harrison J., Omotani J.T., Scannell R., Allan S., Kirk A., Lupelli I. and Thornton A.J. 2015 *Nucl. Fusion* **56** 016006
- [9] Carralero D. et al 2017 *Nucl. Fusion* **57** 056044
- [10] Wynn A. et al 2018 *Nucl. Fusion* **58** 056003
- [11] Vianello N. et al 2020 *Nucl. Fusion* **60** 016001
- [12] Zito A., Wischmeier M., Carralero D., Manz P., Paradela Pérez I. and Passoni M. 2021 *Plasma Phys. Control. Fusion* **63** 075003
- [13] Carralero D. et al 2018 *Nucl. Fusion* **58** 096015
- [14] Wiesen S. et al 2015 *J. Nucl. Mater.* **463** 480
- [15] Bufferand H. et al 2017 *Nucl. Mater. Energy* **12** 852
- [16] Zeiler A., Biskamp D., Drake J.F. and Guzdar P.N. 1996 *Phys. Plasmas* **3** 2951
- [17] Rogers B.N. and Ricci P. 2010 *Phys. Rev. Lett.* **104** 225002
- [18] Tamain P., Bufferand H., Ciralo G., Colin C., Ghendrih P., Schwander F. and Serre E. 2014 *Contrib. Plasma Phys.* **54** 555
- [19] Baudoin C., Tamain P., Bufferand H., Ciralo G., Fedorczak N., Galassi D., Ghendrih P. and Nace N. 2018 *Contrib. Plasma Phys.* **58** 484
- [20] Bufferand H. et al 2021 Implementation of multi-component Zhdanov closure in SOLEDGE3X hal-03243371v2 (Retrieved 25 10 2021)
- [21] Reiter D., Baelmans M. and Börner P. 2005 *Fusion Sci. Technol.* **47** 172
- [22] Bufferand H. et al 2019 *Nucl. Mater. Energy* **18** 82
- [23] Thrysøe A., Madsen J., Naulin V. and Juul Rasmussen J. 2018 *Nucl. Fusion* **58** 096005
- [24] Leddy J., Dudson B. and Willett H. 2017 *Nucl. Mater. Energy* **12** 994
- [25] Zhang D.R., Chen Y.P., Xu X.Q. and Xia T.Y. 2019 *Phys. Plasmas* **26** 012508
- [26] Wersal C. and Ricci P. 2015 *Nucl. Fusion* **55** 123014
- [27] Ricci P., Halpern F.D., Jolliet S., Loizu J., Masetto A., Fasoli A., Furno I. and Theiler C. 2012 *Plasma Phys. Control. Fusion* **54** 124047
- [28] Giacomin M. et al 2021 The GBS code for the self-consistent simulation of plasma turbulence and kinetic neutral dynamics in the tokamak boundary (unpublished)
- [29] Wersal C., Ricci P. and Loizu J. 2017 *Plasma Phys. Control. Fusion* **59** 044011
- [30] Wersal C. and Ricci P. 2017 *Nucl. Fusion* **57** 116018
- [31] Giacomin M., Stenger L. and Ricci P. 2019 *Nucl. Fusion* **60** 024001
- [32] Giacomin M. and Ricci P. 2020 *J. Plasma Phys.* **86** 905860502
- [33] Paruta P., Ricci P., Riva F., Wersal C., Beadle C. and Frei B. 2018 *Phys. Plasmas* **25** 112301
- [34] Ricci P. and Rogers B.N. 2010 *Phys. Rev. Lett.* **104** 145001
- [35] Ricci P. and Rogers B.N. 2013 *Phys. Plasmas* **20** 010702
- [36] Braginskii S. 1965 *Rev. Plasma Phys.* **1** 205
- [37] Zeiler A., Drake J.F. and Rogers B. 1997 *Phys. Plasmas* **4** 2134
- [38] Coda S. et al 2019 *Nucl. Fusion* **59** 112023
- [39] Giacomin M., Stagni A., Ricci P., Boedo J.A., Horacek J., Reimerdes H. and Tsui C.K. 2021 *Nucl. Fusion* **61** 076002
- [40] Stangeby P. 2000 *The Plasma Boundary of Magnetic Fusion Devices (Plasma Physics Series)* (Bristol: IOP Publishing)
- [41] Project T A 2021 Open-adam (<https://open.adam.ac.uk/>)
- [42] Beadle C.F. and Ricci P. 2020 *J. Plasma Phys.* **86** 175860101
- [43] Loizu J., Ricci P., Halpern F.D. and Jolliet S. 2012 *Phys. Plasmas* **19** 122307
- [44] Masetto A., Halpern F.D., Jolliet S., Loizu J. and Ricci P. 2015 *Phys. Plasmas* **22** 012308
- [45] Peterson J.L. and Hammett G.W. 2013 *SIAM J. Sci. Comput.* **35** B576
- [46] Amestoy P.R., Buttari A., L'Excellent J.-Y. and Mary T. 2019 *ACM Trans. Math. Softw.* **45** 1
- [47] Coroado A. and Ricci P. 2021 *Phys. Plasmas* **28** 022310
- [48] Kuang A.Q., LaBombard B., Brunner D., Garcia O.E., Kube R. and Theodorsen A. 2019 *Nucl. Mater. Energy* **19** 295
- [49] Riva F., Militello F., Elmore S., Omotani J.T., Dudson B. and Walkden N.R. (The MAST Team) 2019 *Plasma Phys. Control. Fusion* **61** 095013
- [50] Agostini M. et al 2019 *Plasma Phys. Control. Fusion* **61** 115001
- [51] Carralero D. et al 2014 *Nucl. Fusion* **54** 096015
- [52] Militello F. and Omotani J.T. 2016 *Nucl. Fusion* **56** 104004
- [53] LaBombard B., Boivin R.L., Greenwald M., Hughes J., Lipschultz B., Mossessian D., Pitcher C.S., Terry J.L. and Zweben S.J. 2001 *Phys. Plasmas* **8** 2107
- [54] Rudakov D.L. et al 2005 *Nucl. Fusion* **45** 1589
- [55] Heller M.V.A.P., Brasilio Z.A., Caldas I.L., Stöckel J. and Petrzilka J. 1999 *Phys. Plasmas* **6** 846
- [56] Rudakov D.L. et al 2002 *Plasma Phys. Control. Fusion* **44** 717
- [57] Antar G.Y., Counsell G., Yu Y., Labombard B. and Devynck P. 2003 *Phys. Plasmas* **10** 419
- [58] Nespoli F., Furno I., Labit B., Ricci P., Avino F., Halpern F.D., Musil F. and Riva F. 2017 *Plasma Phys. Control. Fusion* **59** 055009
- [59] Paruta P., Beadle C., Ricci P. and Theiler C. 2019 *Phys. Plasmas* **26** 032302

- [60] Myra J.R., Russell D.A. and D'Ippolito D.A. 2006 *Phys. Plasmas* **13** 112502
- [61] Birkenmeier G. *et al* 2015 *Nucl. Fusion* **55** 033018
- [62] Garcia O.E., Horacek J., Pitts R.A., Nielsen A.H., Fundamenski W., Naulin V. and Rasmussen J.J. 2007 *Nucl. Fusion* **47** 667
- [63] Tsui C.K. *et al* 2021 Evidence on the effects of main-chamber neutrals on density shoulder formation (unpublished)
- [64] Chankina A.V. *et al* 2017 *Nucl. Mater. Energy* **12** 273
- [65] Zhang Y., Krasheninnikov S.I., Masline R. and Smirnov R.D. 2020 *Nucl. Fusion* **60** 106023